Determining the infrared radiative effects of Saharan dust: a radiative transfer modelling study based on vertically resolved measurements at Lampedusa

Daniela Meloni[1], Alcide di Sarra[1], Gérard Brogniez[2], Cyrielle Denjean[3,4], Lorenzo De Silvestri[1], Tatiana Di Iorio[1], Paola Formenti[3], José L. Gómez-Amo[5], Julian Gröbner[6], Natalia Kouremeti[6], Giuliano Liuzzi[7], Marc Mallet[8], Giandomenico Pace[1], Damiano M. Sferlazzo[9]

Correspondence to: Daniela Meloni (daniela.meloni@enea.it)

[1]Laboratory for Observations and Analyses of Earth and Climate, ENEA, Rome, Via Anguillarese 301, 00123, Italy
[2]Laboratoire d'Optique Atmosphérique, University of Lille 1, France
[3]Laboratoire Interuniversitaire des Systèmes Atmosphériques, UMR-CNRS 7583, Université Paris-Est-Créteil et Université Paris Diderot, Institut Pierre Simon Laplace, France
[4]now at Centre National de Recherches Météorologiques, UMR 3589, CNRS, Météo-France, Toulouse, France
[5]Departament de Física de la Terra y Termodinàmica, Universitat de València, Spain
[6]Physikalisch-Meteorologisches Observatorium Davos/World Radiation Center, Davos Dorf, Dorfstrasse 33, 7260, Switzerland
[7]School of Engineering, University of Basilicata, Potenza, Via dell'Ateneo Lucano 10, Italy
[8]CNRM UMR 3589, Météo-France/CNRS, Toulouse, France
[9]Laboratory for Observations and Analyses of Earth and Climate, ENEA, Lampedusa, Contrada Capo Grecale, 92010, Italy

Abstract. Detailed atmospheric and aerosol properties, and radiation measurements were carried out in summer 2013 during the Aerosol Direct Radiative Impact on the regional climate in the MEDiterranean region (ADRIMED) campaign in the framework of the Chemistry-Aerosol Mediterranean Experiment (ChArMEx) experiment. This study focusses on the characterization of infrared (IR) optical properties and direct radiative effects of mineral dust, based on three vertical profiles of atmospheric and aerosol properties and IR broadband and narrowband radiation from airborne measurements, made in conjunction with radiosonde and ground-based observations at Lampedusa, in the central Mediterranean. Satellite IR spectra from IASI are also included in the analysis. The atmospheric and aerosol properties are used as input to a radiative transfer model, and various IR radiation parameters (upward and downward irradiance, nadir and zenith brightness temperature at different altitudes) are calculated and compared with observations. The model calculations are made for different sets of dust size distribution and refractive indices, derived from observations and from the literature. The main results of the analysis are that the IR dust radiative forcing is non negligible, and strongly depends on size distribution (SD) and refractive index (RI). When calculations are made using the *in situ* measured size distribution, it is possible to identify the refractive index that produces the best match with observed IR irradiances and brightness temperatures (BTs). The most appropriate refractive indices correspond to those determined from independent measurements of mineral dust aerosols from the source regions (Tunisia, Algeria, Morocco) of dust transported over Lampedusa, suggesting that differences in the source properties should be taken into account. With the *in situ* size distribution and the most appropriate refractive index the estimated dust IR radiative forcing efficiency is +23.7 W m^{-2} at the surface, -7.9 W m^{-2} within the atmosphere, and +15.8 W m^{-2} at the top of the atmosphere. The use of column integrated dust SD from AERONET may also produce a good agreement with measured irradiances and BTs, but with significantly different values of the RI. This implies large

differences, up to a factor of 2.5 at surface, in the estimated dust radiative forcing, and in the IR heating rate. This study shows that spectrally resolved measurements of brightness temperatures are important to better constrain the dust IR optical properties, and to obtain a reliable estimate of its radiative effects. Efforts should be directed at obtaining an improved description of the dust size distribution, its vertical distribution, and at including regionally-resolved optical properties.

5   **1 Introduction**

Aerosol radiative effects in the infrared or longwave (LW) spectral range have been recognized to be non-negligible compared to that in the solar region for large particles like marine aerosols (e.g. Markowicz et al., 2003) and desert dust (e.g. Vogelmann et al., 2003; Otto et al., 2007; Osborne et al., 2011; di Sarra et al., 2011; Sicard et al., 2014; Meloni et al., 2015 and references therein). The major uncertainty affecting the LW aerosol direct radiative effect (ARF) is due to the

10   poor knowledge of the infrared aerosol optical properties, i.e. the aerosol optical depth, single scattering albedo and phase function.

Desert dust has the largest capability to perturb the IR radiative field, due to the particles' large size and the abundance at the global level, which peaks in the arid regions and their surroundings (Prospero et al., 2002; Ginoux et al., 2012).

Several field campaigns worldwide have been devoted to study the dust microphysical, chemical, and optical properties,

15   with a focus in the infrared radiative effects: Saharan Dust Experiment, SHADE (Highwood et al., 2003), Radiative Atmospheric Divergence using Atmospheric Radiation Measurement (ARM) Mobile Facility, Geostationary Earth Radiation Budget (GERB) data, and African Monsoon Multidisciplinary Analysis (AMMA) stations, RADAGAST (Slingo et al., 2008), Saharan Mineral Dust Experiment, SAMUM (Ansmann et al., 2011), Geostationary Earth Radiation Budget Intercomparison of Longwave and Shortwave radiation, GERBILS (Haywood et al., 2011), NASA AMMA, NAMMA

20   (Hansell et al., 2010), carried out in Africa, Asian Pacific Regional Aerosol Characterization Experiment, ACE-Asia (Seinfeld et al., 2004), and the Asian Monsoon Years field experiment (Hansell et al., 2012) in Asia. Most of these studies have been carried out close to the dust source regions and did not take into account the possible modifications in dust optical properties during long range transport.

A great improvement in the detection of dust in terms of spatial and temporal coverage has been reached after the

25   development of specific algorithms applied to the thermal infrared (TIR) channels of satellite sensors, such as Meteosat (Legrand et al., 2001). More recently, the observations from multichannel sensors, such as MSG-SEVIRI (Schepanski et al., 2007; Brindley and Russell, 2009), high resolution spectrometers like Aqua-AIRS (De Souza-Machado et al., 2006), or interferometers like MetOp-IASI (Peyridieu et al., 2013) have been used to derive dust optical and microphysical properties, taking advantage of the spectral signature of dust in the IR (Clarisse et al., 2013; Cuesta et al., 2015; Sellitto et al., 2016).

30   However, the algorithms developed to infer dust properties from measured brightness temperatures (BT) require that the spectral variation of aerosol extinction, which depends on the spectral complex refractive index (RI) and the particles' size distribution (SD) (Klüser et al., 2012), is known. Thus, understanding the impact of different aerosol optical properties (AOPs) on the infrared BT is crucial for the satellite retrieval. Similarly, IR aerosol optical properties are crucial in determining the LW dust radiative effects in the atmosphere and at the surface (e.g., Meloni et al., 2015).

The Mediterranean Sea is very often affected by dust intrusions from the close Sahara desert (Meloni et al., 2008; Israelevich et al., 2012; Gkikas et al., 2013) producing significant perturbations to the SW and the LW radiation balance (di Sarra et al., 2011; Perrone et al., 2012; Meloni et al., 2015).

Lampedusa island, in the southern portion of the Central Mediterranean, is close to the Tunisian coasts, and hosts the ENEA

5   Station for Climate Observations (35.52° N, 12.63° E, 45 m above sea level), operational since 1997. Due to its position, the small area (22 km^2) and flat surface surrounded by open sea, Lampedusa is an ideal site for the monitoring of transported dust physical and chemical properties. Measurements of aerosol optical depth (AOD) and vertical distribution started in 1999 (Di Iorio et al., 2009; di Sarra et al., 2015); in 2000 Lampedusa became an AERONET (Holben et al., 2001) site. Measurements of downward broadband SW and LW irradiances were started in 2004 (di Sarra et al., 2008; Di Biagio et al.,

10   2010), together with the collection of filters to derive PM10 concentration and chemical composition (Becagli et al., 2012; Marconi et al., 2014).

The Ground based and Airborne Measurements of Aerosol Radiative forcing (GAMARF) field campaign was focussed on the determination of the LW radiative effects of Saharan dust and took place in Lampedusa in spring 2008 (Meloni et al., 2015). The campaign took great advantage from the measured vertical profiles of aerosol SD and LW irradiance from an

15   ultralight aircraft, allowing to derive vertically resolved ARF and aerosol heating rate (AHR) for a case of desert dust intrusion. Moreover, the sensitivity of the SW and LW ARF and AHR to different AOPs was examined.

More recently, Lampedusa also hosted one of the ground-based sites of the Aerosol Direct Radiative Impact on the regional climate in the MEDiterranean region (ADRIMED) field campaign within the Chemistry-Aerosol Mediterranean Experiment (ChArMEx, http://charmex.lsce.ipsl.fr). The ChArMEx/ADRIMED experiment was held from 11 June to 5 July 2013

20   (Mallet et al., 2016). It aimed at characterizing the different aerosol particles and their radiative effect using airborne and ground-based measurements collected in the western and central parts of the basin.

In particular, ChArMEx/ADRIMED deployed two aircrafts based at the Cagliari's airport (Italy), the ATR-42 and Falcon 20, operated by the Service des Avions Français Instrumentés pour la Recherche en Environnement (SAFIRE).

During the campaign, different Saharan dust intrusions were observed at Lampedusa, mainly from 22 to 28 June and from 2

25   to 4 July 2013.

In this paper, we present three case studies, selected to represent desert dust of different load and properties (mainly the vertical profile of the size distribution), and for which airborne measurements are available: 22 and 28 June, and 3 July.

This study contributes at understanding how AOPs determine the LW radiative effects at the surface, in the atmosphere and at the top of the atmosphere, based on the combination of remote sensing and *in situ* observations from the ground, from

30   airborne sensors, and from space, and radiative transfer modelling.

The novel aspect of this study is that the closure experiment is carried out not only on LW irradiance, but also on infrared spectral BT. In particular, the impact of different AOP on the nadir spectral radiances measured by the airborne Conveyable Low-Noise Infrared Radiometer for Measurements of Atmosphere and Ground Surface Targets (CLIMAT) on-board the ATR-42 and IASI and by a ground-based zenith pyrometer is investigated.

35   This paper is organized as follows: an overview of the ground-based, airborne and satellite observations used in the study is given in Sect. 2. Section 3 describes the radiative transfer model set-up and output, with a focus on the choice of the adopted aerosol optical properties. The results of the model calculations and the comparison with measurements are presented in

Sect. 4 in terms of surface irradiance and sky BT, airborne irradiance and BT profiles, and satellite spectral radiance at TOA, with associated uncertainties. Finally, the vertical profiles of ARF and AHR for the 22 June case are discussed.

2 Instruments and measurements

The complete list of the instruments deployed at Lampedusa during the campaign is provided by Mallet et al. (2016), while Denjean et al. (2016) describes the ATR- 42 airborne instruments. Here the instruments and measured parameters used for the radiative closure study are presented.

2.1 Surface observations

Measurements of AOD from the AERONET Cimel standard sunphotometer #172 are available after 17 June 2013, with some interruptions during the campaign. The Multi Filter Rotating Shadowband Radiometer (MFRSR) AOD measurements are also available for the whole time period. The Cimel sunphotometer was calibrated at the AERONET-EUROPE RIMA site in Valladolid just before the campaign, and again in January 2015. The MFRSR is regularly calibrated on site applying the Langley technique, and AOD measurements are corrected by means of empirical functions that take into account the forward scattering caused by desert dust particles, which were derived comparing about four years of simultaneous MFRSR and Cimel measurements at Lampedusa (di Sarra et al., 2015). Here the MFRSR AOD measurements are used because of their higher temporal resolution (about 1 minute) compared to that of the Cimel sunphotometer.

Figure 1 shows the time series of the MFRSR corrected AOD at 500 nm and of the Ångström exponent, α, calculated from the AOD at 500 and 870 nm. The first days of the campaign are characterized by low aerosol load (AOD at 500 nm below 0.15) and small particles (α above 1.5); since 20 June, the aerosol burden increases with a corresponding decrease in α, indicating the arrival of desert dust (Denjean et al., 2016). The peak AOD is reached on 22 June. In the following days the alternation of low and moderate conditions occur, but with α values always below 1.5, suggesting a mixing of particles with different dimensions, including desert dust.

The estimated uncertainty on AOD from a freshly calibrated and well maintained Cimel is ±0.01 for wavelengths larger than 440 nm and ±0.02 below 400 nm (Holben et al., 1998), while that of the MFRSR is <0.02 for the typical conditions at Lampedusa (di Sarra et al., 2015).

The column volume SD is retrieved in 22 size bins between 0.05 and 15 μm (optically equivalent radius) from the Cimel sunphotometer radiance measurements by the inversion method of Dubovik and King (2000). The accuracy of the SD is estimated by Dubovik et al. (2002a) to be below 10% in the maxima and 35% in the minima for particle radii between 0.1 and 7 μm, increasing above 85% outside the interval. Level 2 quality assured inversion products are obtained only for AOD at 440 nm larger than 0.4: this is the case only for the Cimel SD retrieval on 3 July, while on 22 and 28 June Level 1.5 SD are used.

Column-integrated water vapour (IWV) is obtained from the Humidity And Temperature PROfiler (HATPRO), a microwave radiometer developed by Radiometer Physics GmbH (Rose et al., 2005). The instrument measures the sky BT at the high and low-frequency wings of the absorption water vapour and oxygen complex, centred at 22.235 and 60 GHz, respectively. The IWV is derived from the observations in the vertical mode, carried out every second, with a ±0.2

mm uncertainty. Compared to Cimel sunphotometer, the HATPRO provides a much larger dataset with sensibly smaller uncertainties (±1.5 mm for the standard Cimel, according to Holben et al., 2001).

Direct, downward diffuse and global SW irradiance and downward LW irradiance are routinely monitored at Lampedusa. The direct and downward global SW irradiances are measured with a Kipp&Zonen CHP1 pyrheliometer and a CMP21 pyranometer, respectively. The diffuse SW irradiance and the downward LW irradiance are measured with an Eppley PSP pyranometer and a Kipp&Zonen CGR4 pyrgeometer, mounted on a solar tracker with shading balls.

As additional instrumentation deployed during the campaign, the Arctic Radiation Budget Experiment (ARBEX) system from the Physikalisch-Meteorologisches Observatorium Davos/World Radiation Center (PMOD/WRC) was placed on the roof of the building. The ARBEX setup includes Kipp&Zonen CM22 and CM21 pyranometers for downward and upward SW irradiance and Eppley PIR and Kipp&Zonen CG4 pyrgeometers for downward and upward LW irradiance. A modified Kipp&Zonen CGR3 pyrgeometer only sensitive to the 8-14 μm band is also part of ARBEX. All radiometers were freshly calibrated: the modified pyrgeometer with the reference blackbody of the PMOD/WRC at Davos and the broadband ones by comparison with the respective World Standard Groups hosted by the PMOD/WRC in order to guarantee high quality measurements. The measurement uncertainties (one sigma) of a standard and of the modified pyrgeometer calibrated at the WRC are ± 2.3 W m^{-2} and ± 1 W m^{-2}, respectively (Gröbner et al., 2009). Considering the additional uncertainty associated to the data acquisition system (Meloni et al., 2012), an overall two sigma uncertainty on the broadband pyrgeometer measurements of ± 5 W m^{-2} can be assumed. The CGR3 pyrgeometer was not shaded, thus a correction was applied to the measurements in order to remove possible effects due to solar leakage, which was empirically estimated to be proportional to the SW irradiance. This correction causes and additional uncertainty to the CGR3 measurement, that was increased to ± 3 W m^{-2} (one sigma).

The mean bias (with one standard deviation) between the ENEA and the PMOD/WRC pyrgeometers during nighttime periods between June and September 2013 is 1.4 ± 1.2 W m^{-2}, i.e. within the threshold value of ± 2 W m^{-2} defined by Philipona et al. (2001) for well-calibrated instruments.

A KT19.85 II Heitronics Infrared Radiation Pyrometer (IRP) measures the zenith sky BT in the 9.6-11.5 μm spectral interval with a narrow FOV (about 2.6°). The IRP accuracy is estimated as ±0.5 K plus 0.7% of the temperature difference between the instrument body and the observed target (IRP Operational Instructions, 2008). The total accuracy is estimated in ±1 K for the operational conditions of the campaign. The pyrometer is housed in a ventilated box to reduce the measurement degradation due to dirt deposition on the IRP window: for the same reason, the instrument looks at the zenith through a gold mirror. During the campaign the mirror was cleaned every day. The IRP measurements were started on 22 June.

Figure 2 shows the time evolution of the broadband LW irradiance, of the irradiance in the 8-14 μm interval (from now on the WINDOW irradiance), and the infrared zenith BT during the campaign. Although the LW and WINDOW curves follow similar paths, some differences exist due to the different sensitivity of the two instruments to water vapour: the broadband pyrgeometer is sensitive to both IWV and to the water vapour present in the lowest atmospheric layers, while the modified pyrgeometer is mostly sensitive to the IWV. The pyrometer has a minimum detection limit of 223 K, and lower BT values are cut. The BT behaviour resembles that of the irradiances, although some differences are present and are attributed to the different instrumental FOVs, with a larger variability for the IRP BT.

Aerosol backscattering, depolarization, and colour ratio profiles at 532 and 1064 nm wavelengths were obtained by a backscatter lidar developed by the University of Rome "La Sapienza" and ENEA, and operated at Lampedusa since 1998,. The source is a Nd:YAG solid state laser, while the receiving system is composed of various telescopes detecting different altitude ranges in order to retrieve the backscattered signal from about 50 m to the tropopause. The lidar system can be

5   operated in full daylight conditions thanks to the use of narrowband filters and analog signal detection. The details about the instrument set up and the inversion technique are provided by Di Iorio et al. (2009).

Vaisala RS92 radiosondes were launched in conjunction with the flights (not available on 22 June). Top altitudes reached by the sondes were between 25.5 and 33 km.

2.2 Airborne observations

10   The ATR-42 and Falcon 20 flight tracks during the ADRIMED campaign are summarized in Mallet et al. (2016).

In particular, the ADRIMED flights reached Lampedusa during dusty conditions, on 22 and 28 June, and on 2 and 3 July. 22 June and 2 July were the days with the largest AOD values throughout the ADRIMED campaign. The meteorological fields and the maps of dust concentration for the days of the flights are shown and discussed in Denjean et al. (2016).

The ATR-42 sounded the atmosphere during profile descents and ascents; on 22 and 28 June the ATR-42 landed at

15   Lampedusa airport were it refuelled prior to taking off. The Falcon 20 flew above the ATR-42, following paths at nearly constant altitudes. In this study, only data from the descent portions of the ATR-42 flights (respectively, profile F35 on 22 June, F38 on 28 June, and F42 on 3 July) are used, since during the ascents the aircraft attitude is seldom horizontal. The 2 July flight is not analysed since the altitude interval sounded by the ATR-42 is too small to allow radiative closure experiments.

20   Table 1 summarizes the time, average AOD and IWV, and altitudes of the ATR-42 descents and Falcon 20 flights around Lampedusa. The AOD at 500 nm and IWV are mean and standard deviation of the MFRSR and HATPRO measurements within the time duration of the ATR-42 flights.

Aerosol microphysical and optical properties, thermodynamic state of the atmosphere, ozone concentration, downward and upward SW and LW irradiances are measured on-board the ATR-42. SW and LW radiation measurements are also available

25   on-board the Falcon 20.

The aerosol SD at different altitudes in the diameter range 0.03-32 µm is obtained by combining measurements from the Ultra High Sensitivity Aerosol Spectrometer (UHSAS) in the 40-900 nm interval of the optical equivalent diameter, the Grimm 1.129 Optical Particle Counter for diameter sizes from 250 nm to 32 µm, and the Forward Scattering Spectrometer Probe (FSSP) model 300 in the size range 0.28-20 µm (see Denjean et al., 2016 for details). The UHSAS and FSSP

30   spectrometers measure SDs in ambient RH conditions, thus accounting for the possible particle growth due to water uptake.

The radiation instrumentation on-board the ATR-42 and the Falcon 20 includes upward- and downward-looking Kipp&Zonen CMP22 pyranometers and CGR4 pyrgeometers. The upward- and downward- looking instruments are installed above and below the aircraft fuselage, respectively, and are aligned with the aircraft attitude, so that the instrument orientation is determined by the aircraft pitch, roll, and heading angle. The selection of the radiation measurements collected

35   under horizontal position is described in Sect. 4.2. Instruments were calibrated in January 2013. On-board irradiance measurements have been corrected for the aircraft attitude angles (pitch, roll, heading), taking into account also the solar zenith and azimuth angles and the aircraft latitude and longitude, according to Saunders et al. (1992). Other corrections

account for the thermopile response time, the cosine effect, and the temperature dependence of the radiometer's sensitivity. The estimated expanded uncertainties for both components of the instantaneous LW irradiances is ±6 W m^{-2}, obtained taking into account the accuracy of the instrument's calibration and of the acquisition system, and the consistency of airborne measurements.

5   The airborne version of the CLIMAT infrared radiometer (Legrand et al., 2000; Brogniez et al., 2003; 2005; Sourdeval et al., 2012) is installed below the fuselage to measure the nadir BT in three channels centred at 8.7, 10.6, and 12 μm with about 1 μm FWHM bandwidth and about 3° FOV. While the contribution of the O_3 absorption band at 9.6 μm should not affect the CLIMAT measurements in the three bands, the 12 μm channel may be influenced by water vapour and CO_2. The absolute accuracy of BT measurements derived from CLIMAT is about 0.1 K. The instrument was calibrated at the

10   Laboratoire d'Optique Atmosphérique in Febraury 2013.

2.3 Satellite observations

The Infrared Atmospheric Sounder Interferometer (IASI) radiance spectra simultaneous to ground-based measurements have been selected. IASI (Hilton et al., 2012) flies on the two EUMETSAT MetOp A and B polar platforms, with an equator crossing local solar time for the descending node around 9:30 and 8:45, respectively. The interferometer measures

15   the spectral interval from 645 to 2760 cm^{-1}, with a sampling interval of 0.25 cm^{-1} and an effective apodized resolution of 0.5 cm^{-1}, resulting in 8461 points per spectrum. The horizontal resolution at nadir is 12 km. The radiometric noise of IASI spectra is 0.123 K (in the band 780-980 cm^{-1}) and 0.137 K (in the band 1070-1200 cm^{-1}) (Serio et al., 2015). Morning IASI spectra for the days of the campaign are selected in the region including Lampedusa, within the latitude/longitude range 35.0-36.0° N and 12.0-13.2° E. More details can be found in Liuzzi et al. (2017). Clear-sky FOVs

20   are selected applying the Cumulative Discriminant Analysis approach (Amato et al., 2014); data contaminated by sun glint are removed.

3 Radiative transfer model

The MODTRAN release version 5.3 has been used to calculate spectral LW and WINDOW irradiances and BTs at the surface, at aircrafts altitudes, and up to the top of the atmosphere (TOA). The model band highest resolution is 0.2 cm^{-1},

25   allowing to generate accurate spectral transmittances, radiances, and irradiances from 0 to 55000 cm^{-1} (Berk et al., 2006; 2008; Anderson et al., 2009). The DISORT (Stamnes et al., 1988) multiple scattering method with 8 streams with the fast and accurate correlated-k option is used for the simulations in the IR spectral region.

3.1 Model input parameters

30   Pressure, temperature, and relative humidity vertical profiles are obtained from the ATR-42 measurements. At altitudes above the aircraft flight, the radiosounding meteorological parameters and the AFGL standard midlatitude summer profile (Anderson et al., 1986) are used. The time corresponding to the radiosonde launch is reported in Table 1. AFGL profiles of the main absorbing gases (O_3, CH_4, N_2O, CO, CO_2,) are also adopted. The humidity profile is scaled according to the HATPRO IWV averaged over the flight portion, in order to take into account small differences in the radiosonde and the

aircraft paths and time. Column ozone measured at the Station with a Brewer spectrophotometer is used to scale the vertical profile, while surface CO_2 mixing ratio measured with a Picarro G2401 analyser is input to translate the CO_2 AFGL profile. The model vertical resolution used is 0.1 km from the surface to the ATR-42 top altitude (5.8 km on 22 June, 5.4 km on 28 June, 4.8 km on 3 July), 0.25 km up to 10 km, 1 km up to the radiosounding maximum altitude, and larger than 1 km above.

5   Radiosoundings were not launched on 22 June, so data from the European Centre for Medium-Range Weather Forecasts (ECMWF) operational analyses are used, with a spatial resolution of 0.125° x 0.125°. The ECMWF profile closest to the flight F35 (12 UT) is used on 22 June above the ATR-42 altitudes.

The vertical aerosol extinction profile is derived from the lidar backscatter profile and AOD measurements as described in Di Iorio et al. (2009) and Meloni et al. (2015). Figure 3 shows the lidar extinction profile at 532 nm for the three selected

10   cases and the layers identified by the *in situ* aerosol measurements (Denjean et al., 2016).

The infrared emissivity of the sea water from Masuda et al. (1988) has been assumed in the model simulations. The sea emissivity in the 3.5-18 μm window region has been considered for a zenith view and for realistic wind speed. The value at 18 μm is applied also at longer wavelengths. The average surface wind speed is 6.7 m/s for F35, 7.3 m/s for F38, and 4 m/s for F42.

15   Daily MODIS sea surface temperature (SST) data at 1 km resolution (Feldman and McClain, 2014) produced and distributed by the NASA Goddard Space Flight Centre's Ocean Color Data Processing System (OCDPS) have been used.

3.1.1 Aerosol optical properties

The AOPs required by the model are spectral extinction, single scattering albedo, and phase function at each layer. They have been derived from AERONET observations, and from *in situ* measurements on the ATR-42 (Denjean et al., 2016).

20   Figure 4 presents the comparison of AERONET and *in situ* SDs for the three case studies. The *in situ* SDs within the dust layers (LAYER 3 for 22 June and LAYER2 for 3 July) are characterized by a larger number of particles in the large mode compared with the AERONET SD. On 28 June the *in situ* SDs are characterized by lower radii compared to the AERONET SD.

It must be emphasized that a direct comparison of the different SDs is problematic as the AERONET SD is column

25   averaged and is an optically effective distribution essentially derived in the visible spectral range. Moreover, there are limitations in the capability of correctly reproducing the behaviour of the large particles mode, which is primarily important in the desert dust case (see e.g., the smaller accuracy for large particles, Dubovik et al., 2002a). On the contrary, the *in situ* SD is vertically resolved, and thus takes into account differences in aerosol types. On the other hand, small scale effects related to the aircraft position and flight pattern may affect the applicability of the retrieved SD to a somewhat larger scale.

30   Particles' sphericity is assumed in the analysis by Denjean et al. (2016), while the AERONET inversion algorithm that derives the aerosol SD includes spheroid-based parameterization of light scattering (Dubovik et al., 2002b).

No information about the infrared complex RI is available from direct measurements. The Optical Properties of Aerosol and Clouds (OPAC) database (Hess et al., 1998) is widely used as a reference of AOP in the solar and infrared spectral regions for the estimation of aerosol radiative effects (e.g. Gómez-Amo et al., 2014), as well as in the inversion of satellite

35   observations (Klüser et al., 2012). The dust RI from Volz (1973) (Volz1973 from now on) is adopted in various climate models used to evaluate the global dust radiative effect (e.g. Balkanski et al., 2007; Miller et al., 2014).

Recent estimates of the complex refractive index of mineral dust in the infrared spectral region were obtained by Di Biagio et al. (2014a, 2014b; 2017) from different source regions of the world, including Sahara and Sahel deserts. In particular, Di Biagio et al. (2017) (from now on DB2017) have retrieved the RI in the 2-16 μm interval for various samples of natural soil collected in Tunisia, Algeria, and Morocco, which are the most probable source regions of the dust particles detected during

5   the ChArMex flights. Indeed, by comparing air mass back trajectories and dust concentration maps, Denjean et al. (2016) have shown that dust particles were transported from these regions at different altitudes (for details see Table 1 of Denjean et al., 2016); in particular, the dust particles originated from southern Algeria (for altitudes >3500 m) and southern Morocco (1500-3500 m) for profile F35, from Tunisia for profile F38, and from Tunisia (>3000 m) and southern Morocco (<3000 m) for profile F42.

10   The methodology applied in DB2017 allows to estimate the dust RI with an accuracy of about 20% and for conditions resembling the sandblasting process responsible for the generation of dust in the real environment. Moreover, DB2017 suggest that the LW RI does not change due to loss of coarse particles during the transport of dust from the source region, thus enabling its applicability also to transported dust.

The infrared AOPs of dust are henceforth calculated by applying the Mie theory for spherical particles to SD obtained from

15   the AERONET retrieval and the *in situ* observations, and the different RIs from OPAC, Volz1973, and DB2017. The differences in the complex RI from OPAC, Volz1973, and the full group of dust particles studied in DB2017 can be found in Fig. 12 of DB2017.

Below the dust layer (i.e., below 1400 m for F35, below 1000 m for F38, and below 1600 m for F42), the AOPs are calculated using the AERONET and the *in situ* SD and the OPAC water soluble RI.

20   Table 2 summarizes the combination of SD and RI used to obtain the LW AOP. The different combination of SD and RI produces different values of the infrared AOD, reported also in Table 2 at 8.6 μm. The AOD at 8.6 μm is calculated from the MFRSR AOD at 500 nm and the ratio between the extinction coefficient at 8.6 μm and 500 nm obtained from the Mie calculations for each aerosol layer in Fig. 3. On F35 the AOD derived from the *in situ* SDs largely exceeds the AOD obtained with the AERONET SD (for example, by +151% for the OPAC RI). For a fixed SD, the AOD decreases when

25   passing from OPAC to Volz1973 to DB2017 RI. The increase in AOD calculated with the *in situ* SD with respect to the AOD from AERONET SD is also evident for F38 and F42, corresponding to +126% and +81%, respectively.

3.2 Model outputs

The downward and upward broadband LW irradiances are calculated at the surface, at the different atmospheric levels, and at TOA for the different AOPs reported in Table 2. They are compared with the ATR-42, Falcon 20, and ground-based

30   measurements, and with IASI satellite observations.

The CGR3 downward WINDOW irradiance is simulated by integrating the spectral irradiance over the 8-14 μm interval.

The IRP and CLIMAT BTs are obtained integrating the modelled spectral BTs in the respective channel intervals.

The aerosol direct radiative forcing and aerosol heating rates profiles are calculated after simulation of net (downward minus upward) irradiances and heating rates with and without aerosols for each model vertical layer, as in Meloni et al.

35   (2015):

$$ARF(z) = NET_{AER}(z) - NET_{NOAER}(z) \tag{1}$$

$$AHR(z) = -\frac{g}{C_p}\left[\frac{\Delta NET(z)}{\Delta p(z)}\bigg|_{AER} - \frac{\Delta NET(z)}{\Delta p(z)}\bigg|_{NOAER}\right] \tag{2}$$

where z is the altitude, *NET* is the net flux (either SW and LW) with and without aerosols, p is the atmospheric pressure, g the gravitational acceleration, C_p is the specific heat of dry air at constant pressure.

The ARF of the atmosphere is defined as the difference of the ARF at TOA and at the surface.

5 ARF and AHR are estimated only for F35 case, which is characterized by the largest AOD at 500 nm, and thus by the largest LW radiative effects.

The aerosol dust forcing efficiency, ARFE, defined as the ARF per unit AOD at 500 nm, is also calculated at the surface, TOA, and in the atmosphere.

4 Results and discussion

10 **4.1 Surface irradiance and BT**

Ground-based measurements of downward irradiance and BT have been averaged over a 10 minute interval around the time in which the ATR-42 reached the bottom atmospheric layers (see Table 1). The obtained LW and WINDOW irradiances and zenith sky IR BT in the 9.6-11.5 µm band are reported in Table 3.

In the two cases with larger AOD (22 June and 3 July) the AERONET SD is able to reproduce LW irradiance with all RIs

15 (COL1, COL2 and COL3). With the *in situ* SD all RI produce larger irradiances than measurements on 22 June, while on 3 July the agreement with observations depends on the adopted dust RI. The OPAC and Volz1973 RIs (INSU1 and INSU2) produce an overestimate of the irradiances, larger than the measurement uncertainty. The model-measurement difference is within the measurement uncertainty when the DB2017 RI (INSU3) is used. The reasons are twofold: the *in situ* SD of dust has generally a larger number or a larger modal radius of the coarse fraction with respect to AERONET; this implies a

20 stronger infrared emission. On the other hand, the DB2017 RI is characterized by a smaller absorption than OPAC and Volz1973, which produces a smaller dust emission (see Table 2).

On 28 June, the low AOD makes the model results coherent with measurements regardless of the aerosol properties.

Compared to the aerosol-free simulations (NOAER), the smallest perturbation to the surface irradiance and sky BT is produced by the AERONET SD and DB2017 RI (COL3), while the largest effect is produced by INSU1 for all cases.

25 The modelled WINDOW irradiance with aerosol is always overestimated, with the largest overestimate corresponding with the *in situ* SD. As for the broadband LW, the WINDOW irradiance on 22 June can be reproduced with the AERONET SD: the RI yielding the largest (lowest) radiative effect is OPAC (DB2017). On 28 June the modelled WINDOW irradiance is within the measurement uncertainty for the NOAER and the COL3 AOP, i.e. that providing the lowest radiative perturbation. On 3 July the modelled WINDOW irradiance is overestimated with all AOPs and measurements are

30 reproduced only for the NOAER simulations. It should be pointed out that the irradiance in the 8-14 µm interval is very sensitive to the shape of the filter. A sensitive study has been performed reducing the spectral integration by 0.4 µm in different parts of the interval, i.e. considering the 8.2-13.8 µm, the 8.4-14 µm, and the 8-13.6 µm ranges. The INSU3 AOPs have been used for all cases. In all three cases the resulted WINDOW irradiances are considerably reduced (by 8.1, 7.1, and 9.3 W m^{-2}, respectively) with respect to the simulations in the 8-14 µm interval, and are close to the measured values within

35 measurement uncertainty. These results show that for the atmospheric conditions met during the campaign the choice of the

spectral interval for the CGR3 calibration may be critical. This aspect surely deserves a dedicated study, which is beyond the scope of the paper.

On 22 June the zenith sky BT estimated by the model with the AERONET SD is lower than observations, while is generally higher when calculations are made with the *in situ* SD. The combination of *in situ* SD and DB2017 refractive indices

5 produces the best agreement with observations. A similar behaviour is found for 28 June.

The best agreement on 3 July is obtained using the AERONET SD, either for the LW irradiance or for the BT: one possible reason is the absence of *in situ* information on the SD below 1600 m. The same SD as in the 1600-3500 m layer has been assumed in the lowest layers. This assumption may imply inaccurate model simulations using the *in situ* SD. However, as for the first two cases, the simulation with the *in situ* SD with DB2017 RI (INSU3) is sufficiently compliant with the

10 measured LW irradiance and is close to the IRP BT.

Meloni et al. (2015) compared measured and modelled LW irradiances at the surface for a case with low (0.14 on 5 May 2008) and high (0.59 on 3 May 2008) AOD at 500 nm during the GAMARF campaign. Similarly to this work, the simulations were made using SDs derived from AERONET and from *in situ* airborne measurements. For both cases the differences between LW irradiance measurement and model calculations are within measurement uncertainty either without

15 aerosols, and accounting for the aerosol effect with the AERONET and the *in situ* SD. The results of the comparison shown in Table 3 are consistent with those by Meloni et al. (2015): in fact congruity with measurements is obtained either disregarding the aerosol presence, or including aerosols with the AERONET SD (whichever the RI) and with the *in situ* SD, but only on 28 June (all RI) and 3 July (DB2017 RI).

4.2 Airborne irradiance and BT

20 #### 4.2.1 Flight F35

F35 is the descending phase of the ATR-42 flight towards the Lampedusa airport on 22 June. From the flight top (5800 m) down to 3700 m the flight path is above Lampedusa, then the ATR-42 moves East above the open sea while descending close to the surface, down to about 100 m above sea level (see Fig. 5a). Successively, it moves again towards the island before landing: this last part of the descent is not used in the analysis, and only data over the sea are considered.

25 The comparison of the measured and modelled irradiances has been restricted to the 100-5800 m altitude range. Figure 6 shows the measured LW irradiances, selected for pitch and roll angles lower than 1° and 1.5°, respectively, and the model results without aerosol contribution and with all the AOPs. The average AOD during the descent is assumed as model input. The model-measurement comparison is provided in Table 4. The agreement is good for both downward and upward LW irradiances for COL1 and COL2 (RMSD of both components 4.1 W m^{-2}).

30 The NOAER downward LW irradiance profile agrees with observations throughout most of the altitude range, mainly due to the relatively low AOD value. Significant differences are found in the lowest atmospheric layer, where the model including aerosols better fits with observations. Similarly, the aerosol effect on the upward LW irradiance is apparent mainly in the upper altitude range. The aerosol contribution in the LW spectral region due to dust is an increase in the downward LW irradiance at lower altitudes and a decrease in the upward LW irradiances for increasing altitudes.

35 The upward and downward LW irradiances at the Falcon 20 altitude are also reproduced with all AOPs, as shown in Table 5. The downward LW irradiance at the Falcon 20 altitude is not affected by the aerosol AOPs, since the flight altitude is above the aerosol layer top (see Fig. 3). The upward irradiance calculated with the model is within the measurement

uncertainties for both AERONET and *in situ* SD. This confirms the results found for the surface irradiance, i.e. that the broadband irradiance alone cannot help discriminating which SD and RI provide the best representation of the dust optical properties.

The CLIMAT BT profiles are plotted in Fig. 7. BT spikes are associated with ATR-42 passages over the island, where the

5   surface temperature is larger than for the sea. The BT in the upper altitude range is less sensitive to SST, but more affected by the absorption and emission of the bottom layers, including aerosol. Moreover, while SST equally influences the BT at all CLIMAT channels, the spectral variation of the aerosol and atmospheric optical properties produces differences in BT above 2 km altitude. BTs calculated at selected altitudes (600, 3300, 5670 m), corresponding to a nearly horizontal attitude of the ATR-42, are also shown in Fig. 7. Within the dust layer (LAYER 3 in Fig. 3) the occurrence of dust induces a

10   decrease of BT with respect to the aerosol-free cases, with comparable effects for COL1, COL2 and INSU3. A good agreement at all altitudes is observed when aerosols are included, while an overestimation is observed at the highest altitude (5670 m) in the aerosol-free simulation, as also summarized by Table 6. However, while the model-measurement agreement is very good at 600 and 3300 m, where the aerosol impact is small, a systematic overestimation is obtained at 5670 m. The deviation is smaller and not far from the measurement uncertainty for COL1, COL2, and INSU3.

15   These results show that exploring the BT in the thermal infrared is a useful tool to infer dust optical properties if the SD is provided.

Similarly to the upward LW irradiance, the largest BT reduction with respect to aerosol-free conditions occurs above 4 km. The differences in BTs have been calculated for each channel with and without the aerosol contribution: the INSU1 AOPs produce the largest BT reduction at 5650 m (-1.7, -2.0, and -1.7 K at 8.7, 10.6, and 12 μm, respectively), while the lowest

20   reduction is found for COL3 (-0.6, -0.7, and -0.2 K at 8.7, 10.6, and 12 μm, respectively).

For a given SD, the model results obtained with the OPAC and Volz1973 RIs are very similar. Thus, the model simulations for the other two profiles will be made only with the OPAC RI.

4.2.2 Flight F38

As for F35, the F38 profile ends at the Lampedusa airport on 28 June. The descent path to Lampedusa is rather complex

25   (Fig. 5b), with a descending phase from 5420 m down to 3800 m, where the aircraft performed a large circle over the sea (with Lampedusa in the centre) at constant altitude, then continuing the descent. The ATR-42 path overpasses the island at different altitudes (between 600 and 900 m, and between 3500 and 5400 m), and the effect of land emissivity on the upward LW irradiance can be explored.

The AOD at 500 nm measured during the descent is the lowest of the group of three flights (Table 1).

30   Model simulations coded as NOAER, COL1, COL3, INSU1, and INSU3 have been made for this profile.

The downward and upward LW irradiances are plotted in Fig. 8. Overall, the modelled downward LW irradiance follows very well the measured profile. Due to the small AOD, the modelled aerosol effect is small, similar to the irradiance measurement uncertainty. Conversely, differences between model and observations are present in the upward LW irradiance profile, in particular in the 2600-3200 m height range, where the model overestimates measurements by up to 14 W m^{-2}

35   around 2600 m. These differences can not be explained with changes in the temperature and/or humidity profiles, that would have been captured by the airborne instrumentations. In addition, while the upward LW irradiance may be influenced by inhomogeneity in SST or surface emissivity, the SST shows very little variability within the region spanned by the ATR-

42 (two sigma standard deviation less than 1 K in the entire area shown in Fig. 5b and less than 0.3 K in the surface area corresponding to the 2600-3200 m aircraft altitude range).

A large upward LW irradiance variability is observed particularly below 2000 m: for example, the 10 W m^{-2} increase occurring between 1500 and 1700 m cannot be reproduced by the model taking into account the measured atmospheric

5   profiles, nor it can be attributed to the presence of thin clouds, since the humidity is very low (below 20%) in that layer. The ATR-42 flight path shows that at 1700 m the aircraft is close to the West coast of Lampedusa, and the downward-looking pyrgeometer is influenced by the island emission. Similarly, the upward LW irradiance profile shows altitude intervals with sensibly larger values (by about 16-18 W m^{-2}) than the local minima, as around 900 m. The large irradiances correspond to ATR-42 passes over Lampedusa. Model simulations accounting for the island emissivity corroborate this hypothesis.

10   Indeed, the red curve in Fig. 8 is obtained assuming that the surface is a mix of sea (50%) and land (50%), with their respective temperatures. The land temperature is derived from Level 2 MODIS Land Surface Temperature and Emissivity products with 1 km spatial resolution (MOD11_L2). The agreement with measurements at 900 m and at 1700 m confirms that the peak can be attributed to land contribution to the surface emission. A small peak is visible around 4100 m, suggesting that at this altitude the portion of land surface in the pyrgeometer's FOV is smaller than at lower altitudes.

15   The Falcon 20 path is described in Fig. 5b, while the model-measurement comparison is shown in Table 5. The best agreement between modelled and measured upward LW irradiance is obtained with the *in situ* SD. A good agreement is found also with the AERONET SD.

The CLIMAT BTs have been simulated at three different altitudes (700, 3000, and 5200 m) where the ATR-42 is horizontal (Fig. 9). The best agreement between model and measurement is found with the *in situ* SD with minor differences between

20   OPAC and DB2017 RI (INSU1 and INSU3), and with COL1. This is confirmed in Table 6, where the RMSD is below the CLIMAT uncertainty for INSU1. A slight overestimation (0.17 K RMSD) of the model is observed at 3000 m, in agreement with the results for the upward LW irradiance in Fig. 8. Assuming that the differences in BT between model and measurement could be attributed to the SST, their small amount is not sufficient to explain the disagreement in upward LW irradiance. BT simulations without aerosol show that the measured BTs spectral dependence, with nearly equidistant values,

25   is well reproduced by the model. The spike at 900 m indicates that also CLIMAT captures the island emission, while no BT increase is detected at 1700 m, suggesting that while the pyrgeometer 180° FOV collects the signal emitted by the island, the narrow CLIMAT FOV does not.

4.2.3 Flight F42

During flight F42 on 3 July the ATR-42 arrived from north, performed a descent above Lampedusa, at altitudes between

30   4800 and 1600 m, and left southward (Fig. 5c). The short time period of the descent implies negligible AOD variations. As mentioned above, no *in situ* information on the aerosol properties below 1600 m is available.

Figure 10 shows the ATR-42 and the simulated LW irradiance profiles. The agreement between model and measurements for the downward component is good, except for the *in situ* SD and OPAC RI (INSU1), as also shown by the results in Table 4. The model overestimates the upward LW irradiance profile, except at 2000 m, where the aircraft overpassed

35   Lampedusa (see Fig. 5c), and around 4500 m, as also shown by Table 4. On the contrary, a good agreement with all AOPs is found when simulating the Falcon 20 irradiance. This may be a clue for possible inconsistencies in the description of the atmospheric thermodynamic state below the ATR-42 lower altitude, that affect more the simulations at lower altitudes and

less those at higher altitudes. Nonetheless, the CLIMAT BTs (Fig. 11) are well reproduced by the model also at 3000 m, where the upward irradiance is overestimated. Moreover, the underestimation of the CLIMAT BTs at 1600 m is not consistent with the overestimation of the upward irradiance. For these reasons the hypothesis of a bad representation of the thermodynamic profiles in the model is not acceptable. Additionally, non-homogeneities in SST are not evident in the area

5   (two sigma standard deviation of 0.4 K on the whole area of Fig. 5c), which may explain the disagreement of the upward LW irradiance with the model simulations.

The results of Table 6 show that a good model-measurement agreement is found for the AERONET SD and the OPAC RI (COL1), and for the *in situ* SD and DB2017 RI (INSU3). This supports the conclusions of Section 4.2.1, that different combinations of SD and RI may lead to the same values of BT. On the other hand, also in this case the DB2017 RIs appear

10   to produce the best match with observations when the directly measured SD is used.

4.3 IASI radiance simulations

The IASI radiance spectra measured during the morning of 22 and 28 June and 3 July have been considered for the comparison with model simulations. IASI spectra are averaged in a region 1° latitude x 1.2° longitude centred at Lampedusa. The resulting standard deviation on the TOA spectral radiance is around 1% for 22 and 28 June and 0.5% for 3

15   July. A triangular slit function of 0.5 cm^{-1} FWHM has been applied to the simulated spectra in order to reproduce the measured TOA radiances. The AOD at 500 nm and IVW model input have been sampled in a 30-minute interval centred at the time of the IASI observation (8:45 AM for 22 June, 9:06 AM for 28 June, and 9:03 AM for 3 July). Model-measurement differences are calculated in the 8-14 µm interval (714-1250 cm^{-1}), the most significant for evaluating the aerosol effect; the regions of the O_3 (980-1070 cm^{-1}) and CO_2 (below 780 cm^{-1}) absorption bands have been excluded and the comparison

20   evaluated in the 780-980 cm^{-1} and 1070-1200 cm^{-1} intervals, as in Liuzzi et al. (2017), in terms of brightness temperature. The measured and simulated radiance spectra have been resampled at 15 cm^{-1} to reduce the differences due to their respective spectral resolution.

The results of the comparison (Fig. 12) show that differences between model and measurements are larger on 22 June than on 28 June and 3 July. The model shows that dust produces a decrease of the TOA radiance with respect to aerosol-free

25   conditions. The *in situ* SD causes the larger effect compared to the AERONET SD: the maximum reduction of BT in the 780-980 cm^{-1} interval is 1.3 K with COL2 and 2.6 K with INSU2, while in the 1070-1200 cm^{-1} the aerosol-free TOA BT is reduced by 1.1 K with COL2 and by 2.3 K with INSU2. The reduction tends to cancel below 8.5 µm (i.e. above 1176 cm^{-1}) and above 12.5 µm (i.e. below 800 cm^{-1}) because water vapour and carbon dioxide absorption becomes dominant and hides the aerosol effects. On 28 June the amount of the BT reduction is less than 1 K, the largest (lowest) residual obtained with

30   INSU1 (COL3). Similarly to the previous case, on 3 July the perturbation to the TOA aerosol-free radiance reaches 1.1 K with INSU1 in both intervals. Table 7 summarizes the results of the comparison for the two spectral intervals: significant differences with respect to the aerosol-free simulations are obtained with COL1 on 22 June for both intervals, while the best match with the measured spectra is achieved with INSU3 in the 1070-1200 cm^{-1} interval. On 28 June no significant perturbation is produced by the inclusion of the aerosol. The average residual in the 780-980 cm^{-1} interval decreases below

35   the IASI radiometric noise (0.123) with COL3 AOPs. Finally, a significant difference with respect to the aerosol-free simulation is equivalently obtained with COL1 and INSU3, although the best match with the measured BTs between 780 and 980 cm^{-1} is achieved with INSU1. The results in Table 7 suggest that, although the radiative closure at the TOA does

not enable the univocal retrieval of the aerosol RI, the perturbation due to the aerosol effect is significant when the AOD is sufficiently large and that the inclusion of aerosol in the radiative transfer simulations produces a non-marginal improvement of the results.

The model simulations with and without aerosol contribution are very similar for 28 June, due to the low AOD. The aerosol radiative effect is largest on 22 June, either because of the larger AOD and of the aerosol vertical distribution which reaches higher altitudes (Meloni et al., 2005).

Liuzzi et al. (2017) simulated the IASI TOA BT with the σ-IASI-as radiative transfer model using the *in situ* SD and two sets of dust RI, the one from Shettle and Fenn (1979) and those from DB2017. The Shettle and Fenn (1979) RI is very different from the other computed RIs used in this study, especially for the imaginary part, which is considerably lower than that for OPAC and Volz1973, implying lower emission. The real part is also generally lower or Shettle and Fen (1979) compared to OPAC and Volz1973, except for small spectral intervals, like 7-9 μm and 11-19 μm. On the contrary, the AOPs of Liuzzi et al. (2017) using the *in situ* SD are equivalent to INSU3 used here. Other differences in the choice of the model setup and input parameters exist with respect to the present study. First of all, the σ-IASI-as has a finer (0.01 cm^{-1}) resolution than MODTRAN5 (0.1 cm^{-1}). This limitation does not allow to reproduce the high resolution IASI spectra: however, the perturbation to the aerosol-free BT on 22 June with INSU3 AOP (2.3 K at 980 cm-1 and 1.9 K at 1100 cm-1) is comparable to that found in Liuzzi et al. (2017). Furthermore, in Liuzzi et al. (2017) temperature, humidity, and ozone mixing ratio profiles, as well as the sea surface temperature, were taken from the ECMWF reanalyses; in addition, the sea temperature and column water vapour were slightly tuned in order to achieve a better match of the model with IASI spectra. Liuzzi et al. (2017) results show that the best agreement is found with INSU3 for all cases in the 780-980 cm^{-1} band, while Shettle and Fenn (1979) RI seems to perform better in the 1070-1200 cm^{-1} spectral range on 28 June and 3 July. In our case, the MODTRAN spectral resolution impacts the standard deviations of the model-measurement differences, making the results obtained with different AOPs equivalent. It must be however highlighted that our results are obtained without tuning any parameter, by including in the simulations all the available (and significant) observed quantities. The good agreement between model and measurement is thus a quite robust result.

4.4 Radiative forcing and heating rate

The dust LW radiative forcing and heating rate profiles have been estimated for 22 June, which is the case with largest AOD, according to Eq. (1) and (2).

The combination of SD and RI giving the best model-measurement match for the overall set of LW irradiances (downward at surface, upward and downward components on the ATR-42 and Falcon 20) have been evaluated by calculating the RMSD of all model-measurement absolute differences, and selecting only those AOPs for which the RMSD is below the ±5 W m^{-2} threshold value. For the AERONET SD all the three RIs meet the requirement (RMSD between 3.2 and 3.3 W m^{-2}), while for the *in situ* SD only the DB2017 (RMSD 4.7 W m^{-2}).

The ARF and AHR vertical profiles are then calculated with COL1, COL2, COL3, and INSU3 and are shown in Fig. 13. ARF is positive at the surface and at TOA, which corresponds to a higher IR irradiance reaching the surface, and lower irradiance leaving the atmosphere with respect to aerosol-free conditions. A common feature of all profiles is the maximum radiative effect around 3800 m altitude, i.e. below the thickest dust layer (LAYER 3 in Fig. 3), as expected due to dust emission (e.g. Meloni et al., 2015). Very different ARF values are obtained depending on the AOPs, as shown in Table 8.

The largest ARF is produced by INSU3 AOP. The lower DB2017 absorption is evident compared to OPAC and Voltz RIs in the simulations with the AERONET SD. At the surface the ARF for INSU3 is 74% larger than for COL2, and 146% larger than COL3. At TOA the ARF for INSU3 is about 71% larger than for COL2, and 172% larger than for COL3. These large differences show that different combination of SD and RI may all lead to reasonably simulated LW irradiances, but

5   may also produce very different radiative effects. This behaviour underlines the importance of determining accurate AOPs to correctly infer the aerosol radiative effects.

The aerosol dust forcing efficiency ARFE has been calculated at the surface, TOA, and in the atmosphere. The estimated ARFE values are reported in Table 8. The AOPs obtained with the measured SD and the RI giving the best agreement with measured irradiances, which is INSU3, produce the largest ARFE absolute values at the surface, in the atmosphere and at

10   TOA. The ARFE at the surface, +23.7 W m^{-2}, is comparable with the one determined at Lampedusa for the dust event occurring on 3 May 2008 during the GAMARF campaign (Meloni et al., 2015). The ARFE at TOA is nearly doubled with respect to that found during GAMARF, while the atmospheric ARFE is lower. COL1, COL2, and COL3 AOPs provide similar ARFE values, although significantly smaller than for INSU3, at the surface, in the atmosphere and at TOA. The COL3 AOP produces the lowest ARFE at the surface and at TOA, due to the smaller absorption associated with the

15   DB2017 RI compared to OPAC and Volz1973.

The AHR profile is negative within LAYER3, due to cooling caused by dust emission, and becomes positive just below the altitude of the maximum ARF. The layers below 200 m are locally heated by surface emission. Similarly to ARF, the local heating/cooling is very different when considering the various AOPs. For example, the maximum cooling reached at 4400 m is -0.17 Kday^{-1} with INSU3, -0.13 Kday^{-1} with COL1, -0.12 Kday^{-1} with COL2, and -0.08 Kday^{-1} with COL3. Larger

20   differences are observed at the top of LAYER3, around 6200 m, where the AHR with INSU3 is -0.14 Kday^{-1} and decreases to -0.06 Kday^{-1} with COL1 and COL2, and to -0.04 Kday^{-1} with COL3.

5 Conclusions

Three cases of Saharan dust occurring during the summer 2013 ChArMex/ADRIMED campaign have been selected to perform a radiative closure study and to assess how different aerosol optical properties may affect the simulations of various

25   radiation quantities in the infrared spectral interval. The average AOD at 500 nm for the selected cases were moderate: 0.36 on 22 June, 0.21 on 28 June, and 0.26 on 3 July.

Downward surface broadband LW irradiance, irradiance in the 8-14 μm range, and zenith sky BT in the 9.6-11.5 μm band were measured at the ENEA Station for Climate Observations in Lampedusa. Simultaneously, instruments on board the SAFIRE ATR-42 and Falcon 20 aircrafts flying around the island collected vertical profiles of LW irradiance (upward and

30   downward components) and nadir BT in three narrowband channels centred at 8.7, 10.6, and 12 μm. The IASI spectra closest in space and time to the flights have also been selected. In parallel, all parameters influencing the IR radiation were measured or, in some cases, inferred from satellite observations. These include in particular the atmospheric thermodynamic vertical profiles, and the aerosol size distribution.

The MODTRAN5.3 radiative transfer model has been initialized with all the available information. The sensitivity of the

35   computed irradiances and BTs on different aerosol size distributions (columnar from AERONET and *in situ* from airborne observations) and infrared refractive indices (OPAC, Volz1973, and DB2017) has been investigated. The computed IR

AOD (at 8.6 μm) strongly depends on the size distribution: for example, on 22 June the AOD with the *in situ* size distribution increases by a factor of 2.5-2.8 compared to the AOD with the AERONET size distribution, depending on the dust refractive index.

The main results of the study can be summarized in the following points:

1. different combinations of SD and RI may produce similar LW irradiances; more specifically, column integrated SD may produce a good agreement between modelled and observed radiative fluxes with specific values of RI, which however do not necessarily correspond with the occurring value;

2. the integration of *in situ* radiation measurements at different levels in the atmosphere and in different IR bands helps in constraining the aerosol properties and the radiative effects; measurements of broadband LW irradiance
10
are helpful for the determination of the dust properties and radiative effects, but alone do not permit reducing the uncertainty on the dust RI;

3. knowledge of the dust SD, assumed to correspond with the *in situ* vertically resolved profiles, allows to constrain the RI, and consequently aerosol radiative forcing and heating rate. For the ADRIMED campaign, with dust particles originating from northern Algeria, Tunisia and Morocco, the dust RI from DB2017, derived for soil
15
samples from the same regions, produces the best agreement with observations;

4. the use of inaccurate, although optically equivalent, size distributions and refractive indices, has a large impact on the ARF determination. The ARF may change by a factor as large as 2.5 at surface and 2.7 at TOA, depending on the SD and RI, for cases producing a good agreement with observed irradiances. Thus, the knowledge of the SD is crucial for a correct estimate of ARF;
20
5. the values of ARFE retrieved on 22 June are +23.7 W m^{-2} at the surface, -7.9 W m^{-2} in the atmosphere, and +15.8 W m^{-2} at TOA. Significantly smaller ARFE are obtained when equivalent SDs and RIs are used;

6. similarly, the heating rate profile significantly depends on SD, RI, and vertical distribution;

7. knowledge of the whole vertical profile is important to obtain a good closure with respect to the radiative quantities; moreover, the dust vertical distribution appears to influence the derived ARF, primarily at TOA.

The dust radiative effects in the IR are thus non negligible, and their improper estimate may prevent a correct representation of processes acting on local and regional scales. Thus, it appears that specific efforts should be dedicated at determining reliable estimates of the dust vertical distribution and SD, and at implementing source-dependent RIs in regional and large scale models, with the aim of obtaining better determinations of the dust IR radiative effects at the regional scale.

6 Data availability

All the data used in this study are available upon request. Please contact the corresponding author.

The in situ distribution data from the ATR-42 aircraft are available on the ChArMEx database at http://mistrals.sedoo.fr/ChArMEx/. The user must register before having access to the data.

The authors declare that they have no conflict of interest.

Acknowledgements

This work has been supported by the Italian Ministry for University and Research project NextData. Measurements presented here are from the Chemistry-Aerosol Mediterranean Experiment project (ChArMEx, http://charmex.lsce.ipsl.fr), which is the atmospheric component of the French multidisciplinary program MISTRALS (Mediterranean Integrated Studies aT Regional And Local Scales). ChArMEx-France was principally funded by INSU, ADEME, ANR, CNES, CTC (Corsica region), EU/FEDER, Météo-France, and CEA.

The authors thank the Group of Atmospheric Optics, Valladolid University, for the provision of the CÆLIS tool (www.caelis.uva.es) used in this publication and the technicians, pilots and ground crew of SAFIRE (Service des Avions Français Instrumentés pour la Recherche en Environnement) for facilitating the instrument integration and conducting flying operations. We thank the AERONET, PHOTONS and RIMA staff for their support. The research leading to these results has received funding from the European Union Seventh Framework Programme (FP7/2007-2013) under grant agreement Nr. 262254 [ACTRIS].

ECMWF data used in this study have been obtained from the ECMWF Data Server.

The Level 2 MODIS Land Surface Temperature and Emissivity product was retrieved from the online Data Pool, courtesy of the NASA Land Processes Distributed Active Archive Center (LP DAAC), USGS/Earth Resources Observation and Science (EROS) Center, Sioux Falls, South Dakota, https://lpdaac.usgs.gov/data_access/data_pool.

The authors are grateful to Dr. Claudia Di Biagio for providing the dust infrared refractive indices of African soils and for the useful discussion about their use, and to Prof. Carmine Serio and Prof. Guido Masiello for providing the IASI spectra.

References

Anderson, G. P., Clough, S. A., Kneizys, F. X., Chetwynd, J. H., and Shettle, E. P.: AFGL Atmospheric Constituent Profiles (0-120 km), AFGL-TR-86-0110, AFGL (OPI), Hanscom AFB, MA 01736, 1986.

Anderson, G.P., Berk, A., Acharya, P. K., Bernstein, L. S., Adler-Golden, S. M., Lee, J., and Muratov L.: Reformulated Atmospheric Band Model Method for Modeling Atmospheric Propagation at Arbitrarily Fine Spectral Resolution and Expanded Capabilities, U.S. Patent #7593835, issued September 22, 2009.

Ansmann, A., Petzold, A., Kandler, K., Tegen, I., Wendisch, M., Müller, D., Weinzierl, B., Müller, T., and Heintzenberg, J.: Saharan mineral dust experiments SAMUM-1 and SAMUM-2: What have we learned?, Tellus B, 63, 403–429, doi:10.1111/j.1600-0889.2011.00555.x, 2011.

Balkanski, Y., Schulz, M., Claquin, T., and Guibert, S.: Reevaluation of mineral aerosol radiative forcings suggests a better agreement with satellite and AERONET data, Atmos. Chem. Phys., 7, 81–95, doi:10.5194/acp-7-81-2007, 2007.

Becagli, S., Sferlazzo, D. M., Pace, G., di Sarra, A., Bommarito, C., Calzolai, G., Ghedini, C., Lucarelli, F., Meloni, D., Monteleone, F., Severi, M., Traversi, R., and Udisti, R.: Evidence for heavy fuel oil combustion aerosols from chemical analyses at the island of Lampedusa: a possible large role of ships emissions in the Mediterranean, Atmos. Chem. Phys., 12, 3479–3492, doi:10.5194/acp-12-3479-2012, 2012.

Berk, A., Anderson, G. P., Acharya, P. K., Bernstein, L. S., Muratov, L., Lee, J., Fox, M., Adler-Golden, S. M., Chetwynd, J. H., Hoke, M. L., Lockwood, R. B, Gardner, J. A., Cooley, T. W., Borel, C. C., Lewis, P. E., and Shettle, E. P.: MODTRAN5: 2006 Update, Proc. SPIE, Vol. 6233, 62331F, 2006.

Berk, A., Acharya, P. K., Bernstein, L. S., Anderson, G. P., Lewis, P., Chetwynd, J. H., and Hoke, M. L.: Band Model Method for Modeling Atmospheric Propagation at Arbitrarily Fine Spectral Resolution, U.S. Patent #7433806, issued October 7, 2008.

Brindley, H. E. and Russell, J. E.: An assessment of Saharan dust loading and the corresponding cloud-free longwave direct
5   radiative effect from geostationary satellite observations, J. Geophys. Res.-Atmos., 114, D23201, doi:10.1029/2008jd011635, 2009.

Brogniez, G., Pietras, C., Legrand, M., Dubuisson, P., and Haeffelin, M.: A high-accuracy multiwavelength radiometer for in situ measurements in the thermal infrared. Part II: Behavior in field experiments, J. Atmos. Oceanic Technol., 20, 1023–1033, 2003.

10   Brogniez, G., Legrand, M., Damiri, B., Behnert, I., and Buis J.-P.: Multi-channel ground based and airborne infrared radiometers, in: NEWRAD Proc. Ninth Int. Conf. on New Developments and Applications in Optical Radiometry, Davos, Switzerland, Physikalisch- Meteorologisches Observatorium Davos, World Radiation Center, 173–174, 2005.

Clarisse, L., Coheur, P.-F., Prata, F., Hadji-Lazaro, J., Hurtmans, D., and Clerbaux, C.: A unified approach to infrared aerosol remote sensing and type specification, Atmos. Chem. Phys., 13, 2195–2221, doi:10.5194/acp-13-2195-2013, 2013.

15   Cuesta, J., Eremenko, M., Flamant, C., Dufour, G., Laurent, B., Bergametti, G., Hopfner, M., Orphal, J., and Zhou, D.: Three-dimensional distribution of a major desert dust outbreak over East Asia in March 2008 derived from IASI satellite observations, J. Geophys. Res., 120, 7099-7127, 2015.

DeSouza-Machado, S. G., Strow, L. L., Hannon, S. E., and Motteler, H. E.: Infrared dust spectral signatures from AIRS, Geophy. Res. Lett., 33(L03801), 1-5, 2006.

20   Denjean, C., Cassola, F., Mazzino, A., Triquet, S., Chevaillier, S., Grand, N., Bourrianne, T., Momboisse, G., Sellegri, K., Schwarzenbock, A., Freney, E., Mallet, M., and Formenti, P.: Size distribution and optical properties of mineral dust aerosols transported in the western Mediterranean, Atmos. Chem. Phys., 16, 1081-1104, doi:10.5194/acp-16-1081-2016, 2016.

Di Biagio, C., di Sarra, A., and Meloni, D.: Large atmospheric shortwave radiative forcing by Mediterranean aerosols
25   derived from simultaneous ground-based and spaceborne observations and dependence on the aerosol type and single scattering albedo, J. Geophys. Res., 115, D10209, doi:10.1029/2009JD012697, 2010.

Di Biagio, C., Formenti, P., Styler ,S. A., Pangui, E., and Doussin, J.-F.: Laboratory chamber measurements of the longwave extinction spectra and complex refractive indices of African and Asian mineral dusts, Geophys. Res. Lett., 41, 6289–6297, doi:10.1002/2014GL060213, 2014a.

30   Di Biagio, C., Boucher, H., Caquineau, S., Chevaillier, S., Cuesta, J., and Formenti, P.: Variability of the infrared complex refractive index of African mineral dust: experimental estimation and implications for radiative transfer and satellite remote sensing, Atmos. Chem. Phys., 14, 11093-11116, doi:10.5194/acp-14-11093-2014, 2014b.

Di Biagio, C., Formenti, P., Balkanski, Y., Caponi, L., Cazaunau, M., Pangui, E., Journet, E., Nowak, S., Caquineau, S., Andreae, M. O., Kandler, K., Saeed, T., Piketh, S., Seibert, D., Williams, E., and Doussin, J.-F.: Global scale variability of
35   the mineral dust longwave refractive index: a new dataset of in situ measurements for climate modelling and remote sensing, Atmos. Chem. Phys., 17, 1901–1929, doi:10.5194/acp-17-1901-2017 , 2017.

Di Iorio, T., di Sarra, A., Sferlazzo, D. M., Cacciani, M., Meloni, D., Monteleone, F., Fuà, D., and Fiocco, G.: Seasonal evolution of the tropospheric aerosol vertical profile in the central Mediterranean and role of desert dust, J. Geophys. Res., 114, D02201, doi:10.1029/2008JD010593, 2009.

di Sarra, A., Pace, G., Meloni, D., De Silvestri, L., Piacentino, S., and Monteleone, F.: Surface shortwave radiative forcing

5   of different aerosol types in the central Mediterranean, Geophys. Res. Lett., 35, L02714, doi:10.1029/2007GL032395, 2008.

di Sarra, A., Di Biagio, C., Meloni, D., Monteleone, F., Pace, G., Pugnaghi, S., and Sferlazzo D.: Shortwave and longwave radiative effects of the intense Saharan dust event of 25–26 March 2010 at Lampedusa (Mediterranean Sea), J. Geophys. Res., 116, D23209, doi:10.1029/2011JD016238, 2011.

di Sarra, A., Sferlazzo, D., Meloni, D., Anello, F., Bommarito, C., Corradini, S., De Silvestri, L., Di Iorio, T., Monteleone,

10   F., Pace, G., Piacentino, S., and Pugnaghi, S.: Empirical correction of MFRSR aerosol optical depths for the aerosol forward scattering and development of a long-term integrated MFRSR-Cimel dataset at Lampedusa, Appl. Optics, 54, 2725-2737, 2015.

Dubovik, O. and King, M. D.: A flexible inversion algorithm for retrieval of aerosol optical properties from sun and sky radiance measurements, J. Geophys. Res., 105, 20673–20696, 2000.

15   Dubovik, O., Holben, B., Eck, T. F., Smirnov, A., Kaufman, Y. J., King, M. D., Tanre, D., and Slutsker, I.: Variability of Absorption and Optical Properties of Key Aerosol Types Observed in Worldwide Locations, J. Atmos. Sci., 59, 590–608, 2002a.

Dubovik, O., Holben, B. N., Lapyonok, T., Sinyuk, A., Mishchenko, M. I., Yang, P., and Slutsker I.: Non-spherical aerosol retrieval method employing light scattering by spheroids, Geophys. Res. Lett., 29(10), 1415, doi:10.1029/2001GL014506,

20   2002b.

Dutton, E. G. and Long, C., with contributions by Wild, M., Ohmura, A., Gröbner, J., and Roesch, A.: Chapter 5: Long-Term In-Situ Surface Flux Data Products, in GEWEX Radiative Flux Assessment (RFA) Volume 1: Assessment, pp. 135-158, WCRP Report No. 19/2012, World Climate Research Programme, Geneva, Switzerland, 2012. (Available at http://www.wcrp-climate.org/documents/GEWEX%20RFA-Volume%201-report.pdf).

25   Feldman, G. C. and McClain, C. R.: Ocean Color Web, MODIS Reprocessing 5, NASA Goddard Space Flight Center. Eds. Kuring, N., Bailey, S. W. October 2014. http://oceancolor.gsfc.nasa.gov/.

Formenti, P., Rajot, J. L., Desboeufs, K., Caquineau, S., Chevaillier, S., Nava, S., Gaudichet, A., Journet, E., Triquet, S., Alfaro, S., Chiari, M., Haywood, J., Coe, H., and Highwood, E.: Regional variability of the composition of mineral dust from western Africa: Results from the AMMA SOP0/DABEX and DODO field campaigns, J. Geophys. Res., 113, D00C13,

30   doi:10.1029/2008JD009903, 2008.

Ginoux, P., Prospero, J. M., Gill, T. E., Hsu, N. C., and Zhao, M.: Global-scale attribution of anthropogenic and natural dust sources and their emission rates based on MODIS Deep Blue aerosol products, Rev. Geophys., 50, RG3005, doi:10.1029/2012RG000388, 2012.

Gkikas, A., Hatzianastassiou, N., Mihalopoulos, N., Katsoulis, V., Kazadzis, S., Pey, J., Querol, X., and Torres, O.: The

35   regime of intense desert dust episodes in the Mediterranean based on contemporary satellite observations and ground measurements, Atmos. Chem. Phys., 13, 12135–12154, doi:10.5194/acp-13-12135-2013, 2013.

Gómez-Amo, J. L., di Sarra. A., and Meloni. D.: Sensitivity of the atmospheric temperature profile to the aerosol absorption in the presence of dust, Atmos. Environ., 98, 331-336, doi: 10.1016/j.atmosenv.2014.09.008, 2014.

Gröbner, J., Wacker, S., Vuilleumier, L., and Kämpfer, N.: Effective atmospheric boundary layer temperature from longwave radiation measurements, J. Geophys. Res., 114, D19116, doi:10.1029/2009JD012274, 2009.

Hansell, R. A., Tsay, S. C., Ji, Q., Hsu, N. C., Jeong, M. J., Wang, S. H., Reid, J. S., Liou, K. N., and Ou, S. C.: An assessment of the surface longwave direct radiative effect of airborne Saharan dust during the NAMMA field campaign, J.
5   Atmos. Sci., 67, 1048–1065, doi:10.1175/2009JAS3257.1, 2010.

Hansell, R. A., Tsay, S.-C., Hsu, n. C., Ji,Q., Bell, S. W., Holben, B. N., Welton, E. J., Roush, T. L., Zhang, W., Huang, J., Li, Z., and Chen, H.: An assessment of the surface longwave direct radiative effect of airborne dust in Zhangye, China, during the Asian Monsoon Years field experiment (2008), J. Geophys. Res., 117, D00K39, doi:10.1029/2011JD017370, 2012.

10   Haywood, J. M., Johnson, B. T., Osborne, S. R., Mulcahy, J., Brooks, M. E., Harrison, M., Milton, S. F., and Brindley, H.: Observations and modelling of the solar and terrestrial radiative effects of Saharan dust: A radiative closure case-study over oceans during the GERBILS campaign, Q. J. R. Meteorol. Soc., 137, 1211–1226, doi:10.1002/qj.770, 2011.

Hess, M., Koepke, P., and Schult, I.: Optical properties of aerosols and clouds: the software package OPAC, Bull. Amer. Meteorol. Soc., 79, 831-844, 1998.

15   Highwood, E. J., Haywood, J. M., Silverstone, M. D., Newman, S. M., and Taylor, J. P.: Radiative properties and direct effect of Saharan dust measured by the C-130 aircraft during Saharan Dust Experiment (SHADE): 2. Terrestrial spectrum, J. Geophys. Res., 108(D18), 8578, doi:10.1029/2002JD002552, 2003.

Hilton, F., Armante, R., August, T., Barnet, C., Bouchard, A., Camy-Peyret, C., Capelle, V., Clarisse, L., Clerbaux, C., Coheur, P. F., Collard, A., Crevoisier, C., Dufour, G., Edwards, D., Faijan, F., Fourrié, N., Gambacorta, A., Goldberg, M.,
20   Guidard, V., Hurtmans, D., Illingworth, S., Jacquinet-Husson, N., Kerzenmacher, T., Klaes, D., Lavanant, L., Masiello, G., Matricardi, M., McNally, A., Newman, S., Pavelin, E., Payan, S., Péquignot, E., Peyridieu, S., Phulpin, T., Remedios, J., Schlüssel, P., Serio, C., Strow, L., Stubenrauch, C., Taylor, J., Tobin, D., Wolf, W., and Zhou, D.: Hyperspectral Earth Observation from IASI: five years of accomplishments, B. Am. Meteorol. Soc., 93, 347–370, doi:10.1175/BAMS-D-11-00027.1, 2012.

25   Holben B. N., Eck, T. F., Slutsker, I., Tanré, D., Buis, J. P., Setzer, A., Vermote, E., Reagan, J. A., Kaufman, Y. J., Nakajima, T., Lavenu, F., Jankowiak, I., and Smirnov, A.: AERONET - A federated instrument network and data archive for aerosol characterization, Rem. Sens. Environ., 66, 1-16, 1998.

Holben, B., et al.: An emerging ground-based aerosol climatology: Aerosol Optical Depth from AERONET, J. Geophys. Res., 106, 12067–12097, 2001.

30   INFRARED RADIATION PYROMETER KT 19 II, Operational Instruction, Heitronics Infrarot Messtechnik, Version 21/07/08e, pp 3-1.

Israelevich, P., Ganor, E., Alpert, P., Kishcha, P., and Stupp, A.: Predominant transport paths of Saharan dust over the Mediterranean Sea to Europe, J. Geophys. Res., 117, D02205, doi:10.1029/2011JD016482, 2012.

Jin, Z., Qiao, Y., Wang, Y., Fang, Y., and Yi, W.: A new parametrization of spectral and broadband ocean surface albedo,
35   Optics, Express, 19, 26429-26443, 2011.

Klüser, L., Kleiber, P., Holzer-Popp, T., and Grassian, V. H.: Desert Dust Observation From Space – Application of Measured Mineral Component Infrared Extinction Spectra, Atmos. Environ., 54, 419-427, 2012.

Legrand, M., Pietras, C., Brogniez, G., and Haeffelin, M.: A high-accuracy multiwavelength radiometer for in situ measurements in the thermal infrared. Part I: Characterization of the instrument. J. Atmos. Oceanic Technol., 17, 1203–1214, 2000.

Legrand, M., Plana-Fattori, A., and N'doumé, A.: Satellite detection of dust using the IR imagery of Meteosat: 1. Infrared difference dust index, J. Geophys. Res., 106, 18,251 – 18,274, doi:10.1029/2000JD900749, 2001.

Liuzzi, G., Masiello, G., Serio, C., Meloni, D., Di Biagio, C., and Formenti, P.: Consistency of dimensional distributions and refractive indices of desert dust measured over Lampedusa with IASI radiances, Atmos. Meas. Tech., 10,599-615, doi:10.5194/amt-2016-256, 2017.

Mallet, M., Dulac, F., Formenti, P., Nabat, P., Sciare, J., Roberts, G., Pelon, J., Ancellet, G., Tanré, D., Parol, F., Denjean, C., Brogniez, G., di Sarra, A., Alados-Arboledas, L., Arndt, J., Auriol, F., Blarel, L., Bourrianne, T., Chazette, P., Chevaillier, S., Claeys, M., D'Anna, B., Derimian, Y., Desboeufs, K., Di Iorio, T., Doussin, J.-F., Durand, P., Féron, A., Freney, E., Gaimoz, C., Goloub, P., Gómez-Amo, J. L., Granados-Muñoz, M. J., Grand, N., Hamonou, E., Jankowiak, I., Jeannot, M., Léon, J.-F., Maillé, M., Mailler, S., Meloni, D., Menut, L., Momboisse, G., Nicolas, J., Podvin, T., Pont, V., Rea, G., Renard, J.-B., Roblou, L., Schepanski, K., Schwarzenboeck, A., Sellegri, K., Sicard, M., Solmon, F., Somot, S., Torres, B., Totems, J., Triquet, S., Verdier, N., Verwaerde, C., Waquet, F., Wenger, J., and Zapf, P.: Overview of the Chemistry-Aerosol Mediterranean Experiment/Aerosol Direct Radiative Forcing on the Mediterranean Climate (ChArMEx/ADRIMED) summer 2013 campaign, Atmos. Chem. Phys., 16, 455-504, doi:10.5194/acp-16-455-2016, 2016.

Marconi, M., Sferlazzo, D. M., Becagli, S., Bommarito, C., Calzolai, G., Chiari, M., di Sarra, A., Ghedini, C., Gómez-Amo, J. L., Lucarelli, F., Meloni, D., Monteleone, F., Nava, S., Pace, G., Piacentino, S., Rugi, F., Severi, M., Traversi, R., and Udisti, R.: Saharan dust aerosol over the central Mediterranean Sea: PM10 chemical composition and concentration versus optical columnar measurements, Atmos. Chem. Phys., 14, 2039–2054, doi:10.5194/acp-14-2039-2014, 2014.

Markowicz, K. M., Flatau, P. J., Vogelmann, A. M., Quinn, P. K., and Welton, E. J.: Clear-sky infrared radiative forcing at the surface and the top of the atmosphere, Q. J. Roy. Meteor. Soc. 129, 2927–2947, 2003.

Masuda, K., Takashima, T., and Takayama, Y.: Emissivity of pure and sea waters for the model sea surface in the infrared window regions, Remote Sens. Environ., 24, 313–329, 1988.

Meloni, D., di Sarra, A., Di Iorio, T., and Fiocco, G.: Influence of the vertical profile of Saharan dust on the visible direct radiative forcing, J. Quant. Spectrosc. Radiat. Transfer, 93, 397–413, 2005.

Meloni, D., Di Biagio, C., di Sarra, A., Monteleone, F., Pace, G., and Sferlazzo, D. M.: Accounting for the solar radiation influence on downward longwave irradiance measurements by pyrgeometers, J. Atmos. Oceanic Technol., 29(11), 1629–1643, 2012.

Meloni, D., Junkermann, W., di Sarra, A., Cacciani, M., De Silvestri, L., Di Iorio, T., Estellés, V., Gómez-Amo, J. L., Pace, G., and Sferlazzo, D. M.: Altitude-resolved shortwave and longwave radiative effects of desert dust in the Mediterranean during the GAMARF campaign: Indications of a net daily cooling in the dust layer, J. Geophys. Res. Atmos., 120, 3386–3407, doi:10.1002/2014JD022312, 2015.

Miller, R. L., Knippertz, P., Pérez García-Pando, C., Perlwitz, J. P., and Tegen, I.: Impact of dust radiative forcing upon climate, in: Mineral Dust: A Key Player in the Earth System. P. Knippertz, and J.-B.W. Stuut, Eds. Springer, 327-357, doi:10.1007/978-94-017-8978-3_13, 2014.

Osborne, S. R., Baran, A. J., Johnson B. T., Haywood, J. M., Hesse, E., and Newman, S.: Short-wave and long-wave radiative properties of Saharan dust aerosol, Q. J. Roy. Meteorol. Soc., 137, 1149–1167, doi:10.1002/qj.771, 2011.

Otto, S., de Reus, M., Trautmann, T., Thomas, A., Wendisch, M., and Borrmann, S.: Atmospheric radiative effects of an in situ measured Saharan dust plume and the role of large particles, Atmos. Chem. Phys. 7, 4887–4903, doi:10.5194/acp-7-4887-2007, 2007.

Perrone, M. R., Tafuro, A. M., and Kinne, S.: Dust layer effects on the atmospheric radiative budget and heating rate profiles, Atmos. Environ., 59, 344-354, 2012.

Peyridieu, S., Chedin, A., Capelle, V., Tsamalis, C., Pierangelo, C., Armante, R., Crevoisier, C., Crepeau, L., Simeon, M., Ducos, F., and Scott, N. A.: Characterisation of dust aerosols in the infrared from IASI and comparison with PARASOL, MODIS, MISR, CALIOP, and AERONET observations, Atmos. Chem. Phys., 13, 6065–6082, doi:10.5194/acp-13-6065-2013, 2013.

Philipona, R., Dutton, E. G., Stoffel, T., Michalsky, J., Reda, I., Stifter, A., Wendling, P, Wood, N., Clough, S. A., Mlawer, E. J., Anderson, G., Revercomb, H. E., and Shippert, T. R.: Atmospheric longwave irradiance uncertainty: Pyrgeometers compared to an absolute sky-scanning radiometer, atmospheric emitted radiance interferometer, and radiative transfer model calculations, J. Geophys. Res. 106, 28129-28141, 2001.

Prospero, J. M., Ginoux, P., Torres, O., Nicholson, S. E., and Gill, T. E.: Environmental characterization of global sources of atmospheric soil dust identified with the Nimbus 7 Total Ozone Mapping Spectrometer (TOMS) absorbing aerosol product, Rev. Geophys., 40, 2-1–2-31, 2002.

Rose, T., Crewell, S., Löhnert, U., and Simmer, C.: A network suitable microwave radiometer for operational monitoring of the cloudy atmosphere, Atmos. Res., 75, 183-200, 2005.

Saunders, R. W., Brogniez, G., Buriez, J. C., Meerkotter, R., and Wendling, P: A comparison of Measured and Modeled Broadband Fluxes from Aircraft Data during the ICE '89 Field Experiment, J. Atmos. Oceanic Technol., 9, 391–406, 1992.

Schepanski, K., Tegen, I., Laurent, B., Heinold, B., and Macke, A.: A new Saharan dust source activation frequency map derived from MSG-SEVIRI IRchannels, Geophys. Res. Lett., 34, L18803, doi:10.1029/2007GL030168, 2007.

Seinfeld, J. H., Carmichael, G. R., Arimoto, R., Conant, W. C., Brechtel, F. J., Bates, T. S., Cahill, T. A., Clarke, A. D., Doherty, S. J., Flatau, P. J., Huebert, B. J., Kim, J., Markowicz, K. M., Quinn, P. K., Russell, L. M., Russell, P. B., Shimizu, A., Shinozuka, Y., Song, C. H., Tang, Y., Uno, I., Vogelmann, A. M., Weber, R. J., Woo, J.-H., and Zhang, X. Y.: ACE-ASIA regional climatic and atmospheric chemical effects of Asian dust and pollution, B. Am. Meteorol. Soc., 85, 367–380, 2004.

Sellitto, P. and Legras, B.: Sensitivity of thermal infrared nadir instruments to the chemical and microphysical properties of UTLS secondary sulfate aerosols, Atmos. Meas. Tech., 9, 115-132, doi:10.5194/amt-9-115-2016, 2016.

Serio, C., Standfuss, C., Masiello, G., Liuzzi, G., Dufour, E., Tournier, B., Stuhlmann, R., Tjemkes, S., and Antonelli, P.: Infrared Atmospheric Sounder Interferometer radiometric noise assessment from spectral residuals, Appl. Opt., 54(19), 5924–5936, doi:10.1364/AO.54.005924, 2015.

Sicard, M., Bertolín, S., Mallet, M., Dubuisson, P., and Comerón, A.: Estimation of mineral dust longwave radiative forcing: Sensitivity study to particle properties and application to real cases in the region of Barcelona, Atmos. Chem. Phys., 14, 9213–9231, doi:10.5194/acp-14-9213-2014, 2014.

Slingo, A., et al.: Overview of observations from the RADAGAST experiment in Niamey, Niger: Meteorology and

thermodynamic variables, J. Geophys. Res., 113, D00E01, doi:10.1029/2008JD009909, 2008.

Sokolik, I. and Toon, O.: Incorporation of mineralogical composition into models of the radiative properties of mineral aerosol from UV to IR wavelengths, J. Geophys. Res., 104, 9423–9444, 1999.

Sourdeval, O. and Brogniez, G.: Validation of IIR/CALIPSO Level 1 Measurements by Comparison with Collocated

5   Airborne Observations during CIRCLE-2 and Biscay '08 Campaigns, J. Atmos. Oceanic Technol., 29, 653-667, 2012.

Stamnes, K., Tsay, S.-C., Wiscombe, W., and Jayaweera, K.: Numerically stable algorithm for discrete-ordinate-method radiative transfer in multiple scattering and emitting layered media, Appl. Optics, 27, 2502–2509, doi:10.1364/AO.27.002502, 1988.

Vogelmann, A., Flatau, P., Szczodrak, M., Markowicz, K., and Minnett, P.: Observations of large aerosol infrared forcing at

10   the surface, Geophys. Res. Lett., 30, 1655, doi:10.1029/2002GL016829, 2003.

Volz, F. E.: Infrared optical constants of ammonium sulfate, Sahara dust, volcanic pumice and flyash, Appl. Optics, 12, 564-568, 1973.

Table 1. Summary of the time intervals, average (with standard deviation) AOD at 500 nm, IWV, and surface temperature during the descent portion of the three flights selected for this study. The altitude ranges of the ATR-42 and Falcon 20 observations are also shown.

Day/Flight	Time (UT)	Radiosonde launch time (UT)	AOD at 500 nm	IWV (cm)	Surface T (K)	ATR-42 altitude range (m)	Falcon 20 altitude range (m)
22/06 F35	10:23-11:18	n. a.	0.36±0.01	2.65±0.04	298.5±0.1	5800-15	10555-10565
28/06 F38	12:25-13:30	11:30	0.21±0.01	2.19±0.02	296.0±0.1	5420-15	9530-9560
03/07 F42	9:47-10:01	11:31	0.259±0.006	3.02±0.01	298.5±0.1	4830-1600	9280-9310

Table 2. Summary of the size distributions and complex refractive indices combinations used to calculate AOPs in the infrared spectral interval. The abbreviations for each combination and for aerosol-free conditions are reported in the first column. Average AOD at 8.6 µm for each profile (F35, F38, F42).

Abbreviation	Size distribution (SD)	Refractive index (RI)	AOD F35	AOD F38	AOD F42
NOAER	No aerosol				
COL1	AERONET	Dust layer: OPAC mineral (Hess et al., 1998)	0.058	0.031	0.043
		Below the dust layer: OPAC water soluble (Hess et al., 1998)			
COL2	AERONET	Dust layer: Saharan dust (Volz, 1973)	0.055		
		Below the dust layer: OPAC water soluble (Hess et al., 1998)			
COL3	AERONET	Dust layer: Algeria-Tunisia-Morocco dust (Di Biagio et al., 2017)	0.040	0.023	0.032
		Below the dust layer: OPAC water soluble (Hess et al., 1998)			
INSU1	*in situ*	Dust layer: OPAC mineral (Hess et al., 1998)	0.146	0.070	0.078
		Below the dust layer: OPAC water soluble (Hess et al., 1998)			
INSU2	*in situ*	Dust layer: Saharan dust (Volz, 1973)	0.135		
		Below the dust layer: OPAC water soluble (Hess et al., 1998)			
INSU3	*in situ*	Dust layer: Algeria-Tunisia-Morocco dust (Di Biagio et al., 2017)	0.110	0.061	0.064
		Below the dust layer: OPAC water soluble (Hess et al., 1998)			

Table 3. Measured and simulated downward LW and WINDOW irradiance and sky BT at the surface for the three analysed cases; model calculations are performed with different AOPs. The measurement uncertainty is shown in parentheses together with the measured values. The model-measurement difference is shown in parentheses together with the modelled values. Differences within the measurement uncertainty are in bold.

AOP	NOAER	COL1	COL2	COL3	INSU1	INSU2	INSU3	Measurement
22 June								
LW (W m^{-2})	356.3	361.1	361.0	359.6	367.2	366.9	364.4	358.6 (±5)
	(-2.3)	**(+2.5)**	**(+2.4)**	**(+1.0)**	(+8.6)	(+8.3)	(+5.8)	
WINDOW (W m^{-2})	82.5	87.3	87.2	85.8	93.4	93.1	90.5	81.3 (±6)
	(+1.2)	**(+6.0)**	**(+5.9)**	**(+4.5)**	(+12.1)	(+11.8)	(+9.2)	
IR BT (K)	224.2	228.4	229.1	227.5	234.2	234.6	232.5	231.9 (±1)
	(-7.7)	(-3.5)	(-2.8)	(-4.4)	(+2.3)	(+2.7)	**(+0.6)**	
28 June								
LW (W m^{-2})	335.2	338.6		336.9	341.5		339.3	337.9 (±5)
	(-2.7)	**(+0.5)**		**(-1.0)**	**(+3.6)**		**(+2.4)**	
WINDOW (W m^{-2})	73.4	76.7		75.1	79.5		77.4	70.6 (±6)
	(+2.8)	(+6.1)		**(+4.5)**	(+8.9)		(+6.8)	
IR BT (K)	219.9	223.0		221.6	225.9		224.2	224.8 (±1)
	(-4.9)	(-1.8)		(-3.2)	(+1.1)		**(-0.6)**	
3 July								
LW (W m^{-2})	362.4	367.4		365.6	370.8		368.0	363.7 (±5)
	(-1.3)	**(+3.7)**		**(+1.9)**	(+7.1)		**(+4.3)**	
WINDOW (W m^{-2})	92.0	96.9		95.1	100.1		97.4	86.8 (±6)
	(+5.2)	(+10.1)		(+8.3)	(+13.3)		(+10.6)	
IR BT (K)	233.6	237.4		236.1	240.5		238.2	237.0 (±1)
	(-3.4)	**(+0.4)**		**(-0.9)**	(+3.5)		(+1.2)	

Table 4. RMSD in W m^{-2} between modelled and measured downward and upward LW irradiances for the ATR-42 profiles in the three analysed cases. Model calculations are made with different AOPs. The measurement uncertainty is ±6 W m^{-2}. Values within the measurement uncertainty are in bold.

AOP	NOAER	COL1	COL2	COL3	INSU1	INSU2	INSU3
			22 June				
LW↓	**3.4**	**3.2**	**3.0**	**2.2**	9.3	8.8	**5.6**
LW↑	**5.9**	**4.9**	**4.9**	**5.2**	**3.9**	**4.0**	**4.4**
			28 June				
LW↓	**3.8**	**3.2**		**3.5**	**3.4**		**3.2**
LW↑	7.7	7.2		7.4	6.8		7.0
			3 July				
LW↓	**4.0**	**5.9**		**4.8**	7.2		**5.6**
LW↑	10.9	9.2		9.6	8.6		9.1

Table 5. Downward and upward LW irradiances measured on-board the Falcon 20 and modelled for on the three analysed cases. Model calculations are made with different AOPs. The measurements uncertainty is ±6 W m^{-2}. Differences with respect to measurements are shown in parentheses and are in bold if lower than the measurement uncertainty.

AOP	NOAER	COL1	COL2	COL3	INSU1	INSU2	INSU3	Measurement
22 June								
LW↓	41.0	41.0	41.0	41.0	41.0	41.0	41.0	42.7
	(-1.7)	**(-1.7)**	**(-1.7)**	**(-1.7)**	**(-1.7)**	**(-1.7)**	**(-1.7)**	
LW↑	298.0	294.1	294.3	295.6	288.9	289.2	291.7	293.2
	(+4.8)	**(+0.9)**	**(+1.1)**	**(+2.4)**	**(-4.3)**	**(-4.0)**	**(-1.5)**	
28 June								
LW↓	51.2	51.2		51.2	51.2		51.2	56.2
	(-5.0)	(-5.0)		(-5.0)	(-5.0)		(-5.0)	
LW↑	300.0	298.6		299.2	297.2		298.0	293.1
	(+6.9)	**(+5.5)**		(+6.1)	**(+4.1)**		**(+4.9)**	
3 July								
LW↓	57.0	57.0		57.0	57.0		57.0	56.8
	(+0.2)	**(+0.2)**		**(+0.2)**	**(+0.2)**		**(+0.2)**	
LW↑	306.6	304.9		305.7	303.6		304.8	301.9
	(+4.7)	**(+3.0)**		**(+3.8)**	**(+1.7)**		**(+2.9)**	

Table 6. Comparison of the measured and modelled CLIMAT BTs. Model calculations are made with different AOPs. Differences are expressed as RMSD (K) from data at three different altitudes and for the three CLIMAT channels (see text). The RMSD at the maximum altitude is shown in parentheses.

AOP	NOAER	COL1	COL2	COL3	INSU1	INSU2	INSU3
22 June	0.36 (0.61)	0.10 (0.15)	0.11 (0.17)	0.19 (0.32)	0.27 (0.47)	0.25 (0.43)	0.10 (0.16)
28 June	0.27 (0.36)	0.14 (0.15)		0.21 (0.27)	0.09 (0.09)		0.12 (0.11)
3 July	0.22 (0.23)	0.17 (0.02)		0.19 (0.14)	0.21 (0.16)		0.18 (0.03)

Table 7. Differences (K) between modelled and measured IASI BT spectra in the 780-980 cm^{-1} and 1070-1200 cm^{-1} spectral intervals of the atmospheric window. Model calculations with different AOPs are shown. Differences are expressed as percent RMSD and standard deviation. In bold the significant differences with respect to the NOAER simulations.

AOP	NOAER	COL1	COL2	COL3	INSU1	INSU2	INSU3
			22 June				
780-980 cm^{-1}	1.0±0.3	**0.4±0.3**	0.5±0.5	0.7±0.3	1.1±0.4	1.5±0.8	0.8±0.6
1070-1200 cm^{-1}	1.3±0.3	**0.6±0.1**	**0.6±0.2**	**0.8±0.1**	**0.4±0.3**	0.8±0.7	**0.2±0.2**
			28 June				
780-980 cm^{-1}	0.2±0.1	0.2±0.1		0.1±0.1	0.5±0.1		0.3±0.1
1070-1200 cm^{-1}	0.5±0.2	0.3±0.2		0.4±0.2	0.2±0.2		0.2±0.2
			3 July				
780-980 cm^{-1}	0.8±0.1	**0.4±0.2**		0.6±0.2	**0.2±0.2**		**0.4±0.2**
1070-1200 cm^{-1}	0.9±0.1	**0.6±0.2**		0.7±0.2	0.5±0.4		**0.6±0.2**

Table 8. LW ARF and ARFE at the surface, TOA, and in the atmosphere (in W m^{-2}) on 22 June calculated with the AOPs which produce the best agreement with respect to the irradiance profiles.

AOP	ARF				ARFE			
	COL1	COL2	COL3	INSU3	COL1	COL2	COL3	INSU3
Surface	5.0	4.9	3.5	8.5	13.9	13.6	9.6	23.7
TOA	3.5	3.3	2.1	5.7	9.7	9.2	5.8	15.8
Atmosphere	-1.5	-1.6	-1.4	-2.8	-5.8	-5.6	-3.8	-7.9
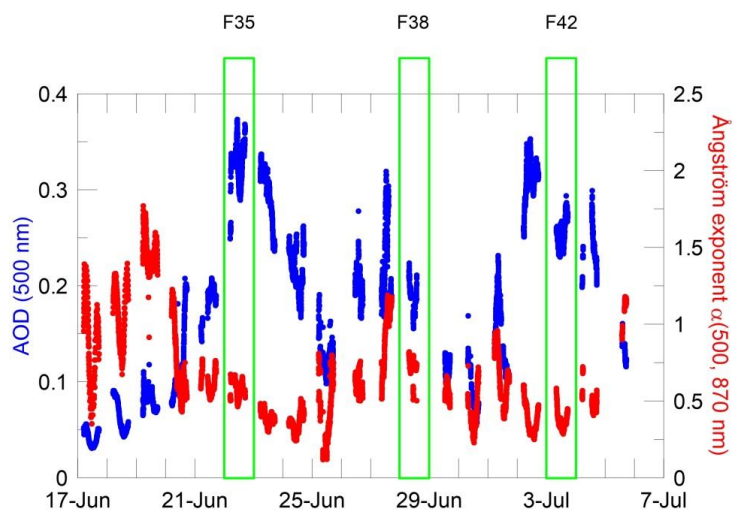
Figure 1: AOD at 500 nm (blue dots) and Ångström exponent (red dots) measured by the MFRSR during the campaign.
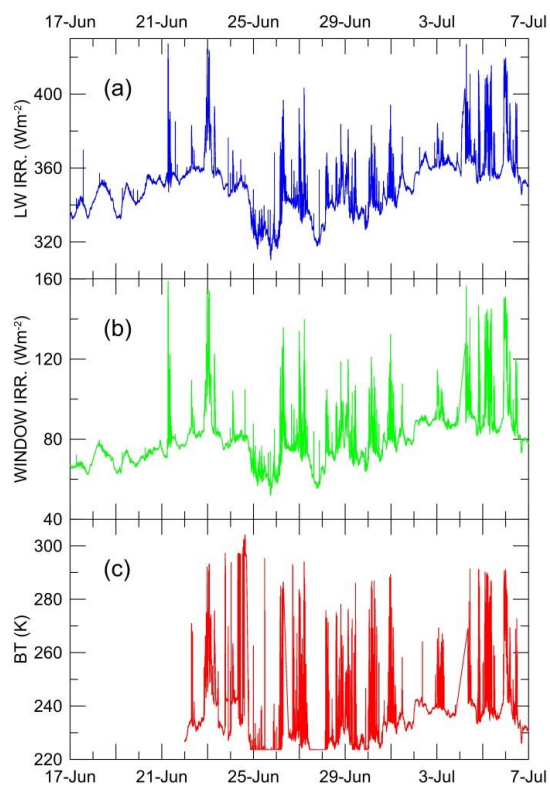
Figure 2: Time evolution of (a) the downward broadband LW irradiance, (b) the WINDOW irradiance, and (c) the zenith sky BT during the ADRIMED campaign.
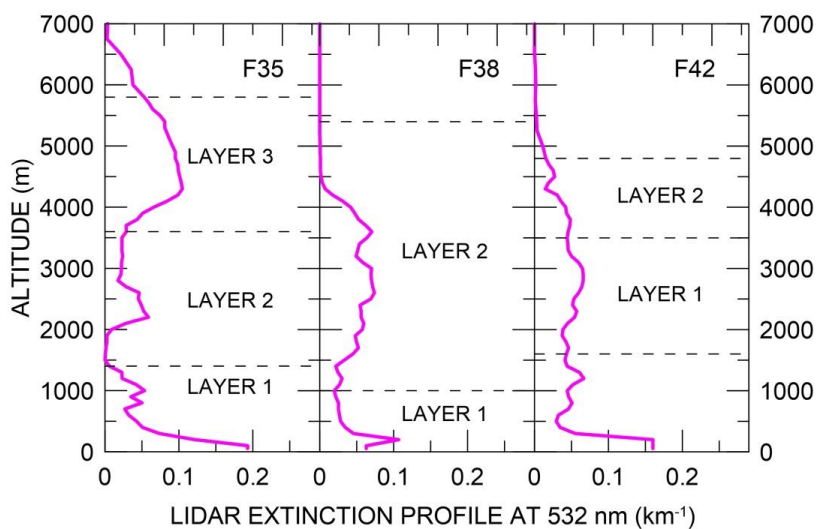
Figure 3: Lidar extinction profiles at 532 nm averaged during the three ATR-42 descents. From left to right, on 22 and 28 June, and on 3 July. The aerosol layers identified by different optical properties from the *in situ* airborne measurements are also evidenced. Note that on 3 July the *in situ* profiles end at the bottom of layer 1.
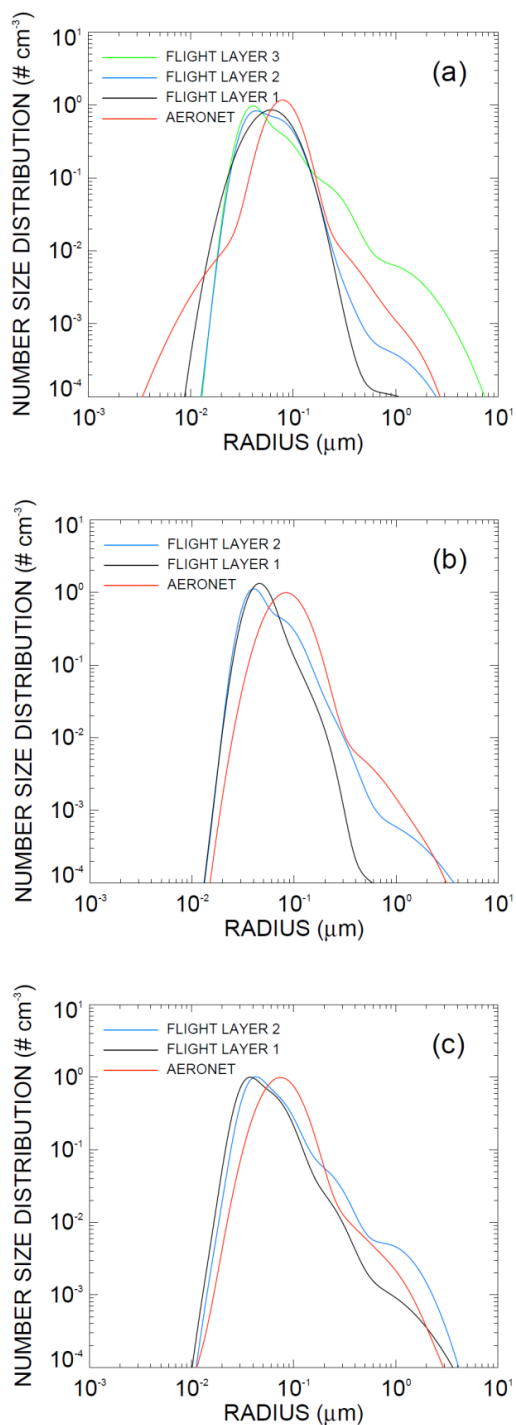
Figure 4: Normalized aerosol number size distribution derived from AERONET measurements (red curve) and from the airborne in situ measurements for the layers of figure 3 for (a) F35, (b) F38, and (c) F42.
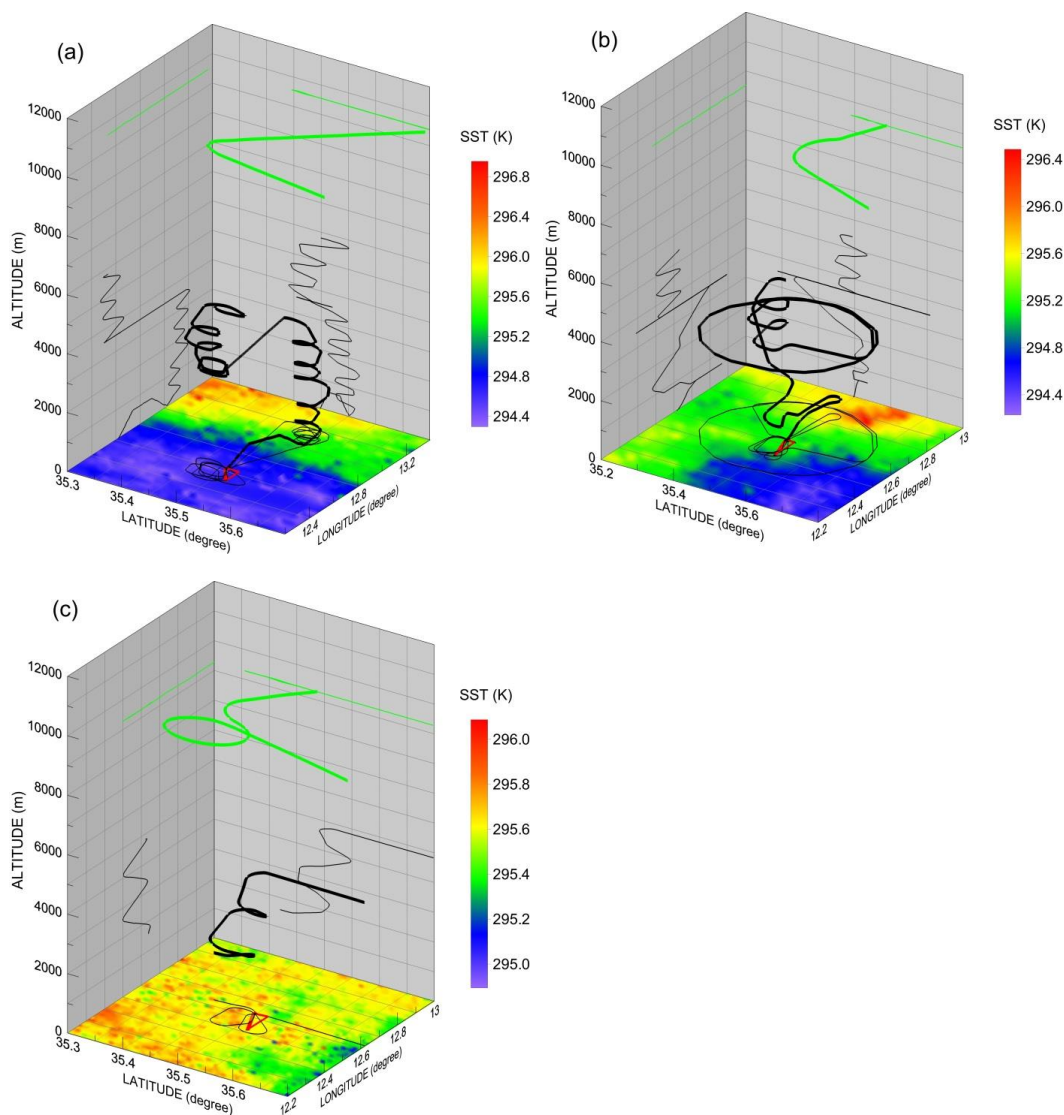
Figure 5: ATR-42 (black curve) and Falcon 20 (green curve) flight paths on (a) 22 June (F35), (b) 28 June (F38), and (c) 3 July
5   **(F42), and projections on horizontal and vertical planes. The surface map of the SST from MODIS is shown with the colour scale. A schematic map of Lampedusa contour is shown in red. Please, note that the latitude-longitude and the SST scales are different in each graph.**
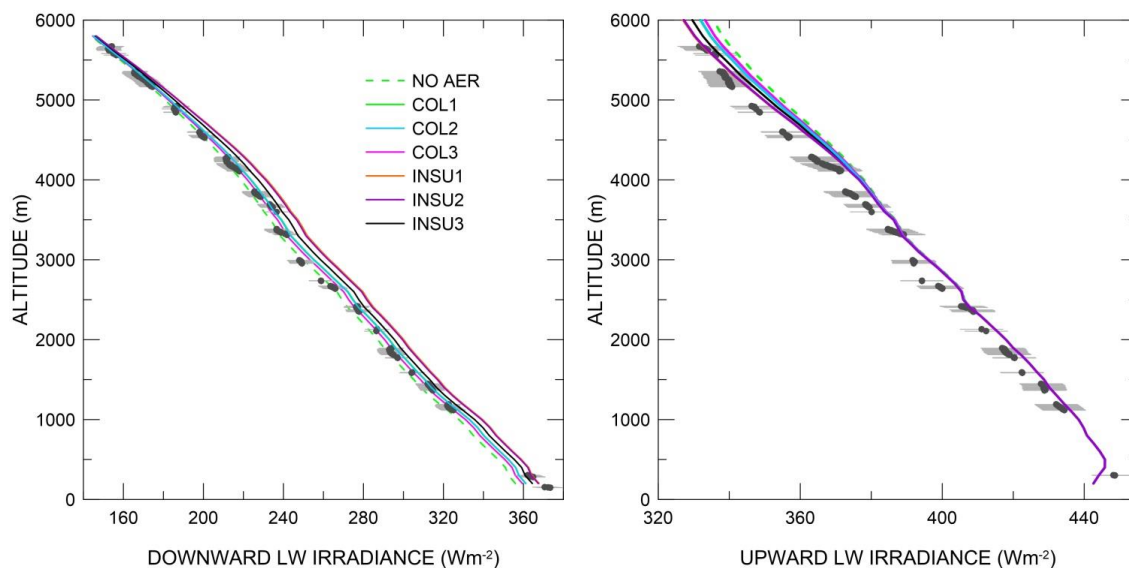
Figure 6: Downward (left) and upward (right) LW irradiance profiles for F35. Grey dots are the measurements selected for small pitch and roll angles, with the associated uncertainty (one sigma) in light grey. Simulated profiles with different SDs and RIs are shown in different colours. See text for details.
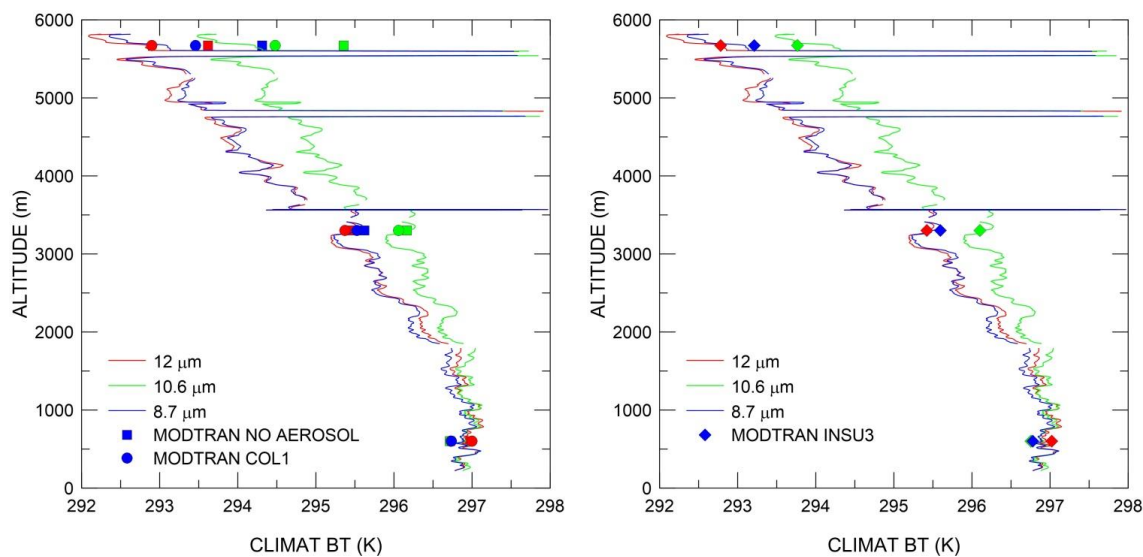
Figure 7: CLIMAT BTs vertical profiles and simulated BTs at selected altitudes during F35 for aerosol-free conditions and with different AOPs: AERONET SD and OPAC RI (left) and *in situ* SD and Algerian and Moroccan dust RIs (right).
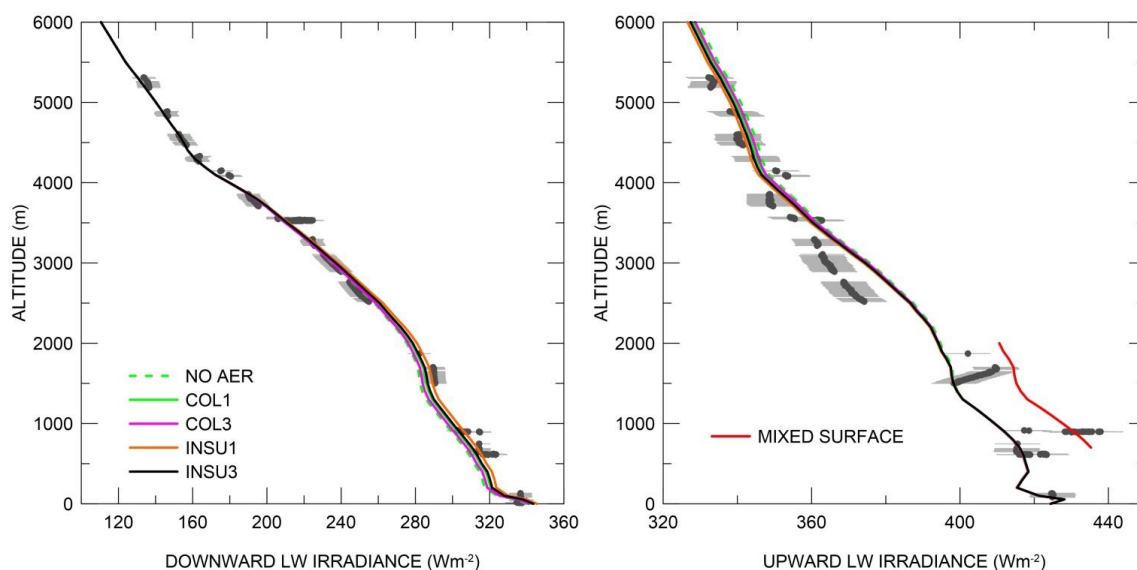
Figure 8: Same as Figure 6, but for profile F38. The red curve in the upward LW irradiance plot is obtained using Lampedusa surface temperature and emissivity. See text for details.
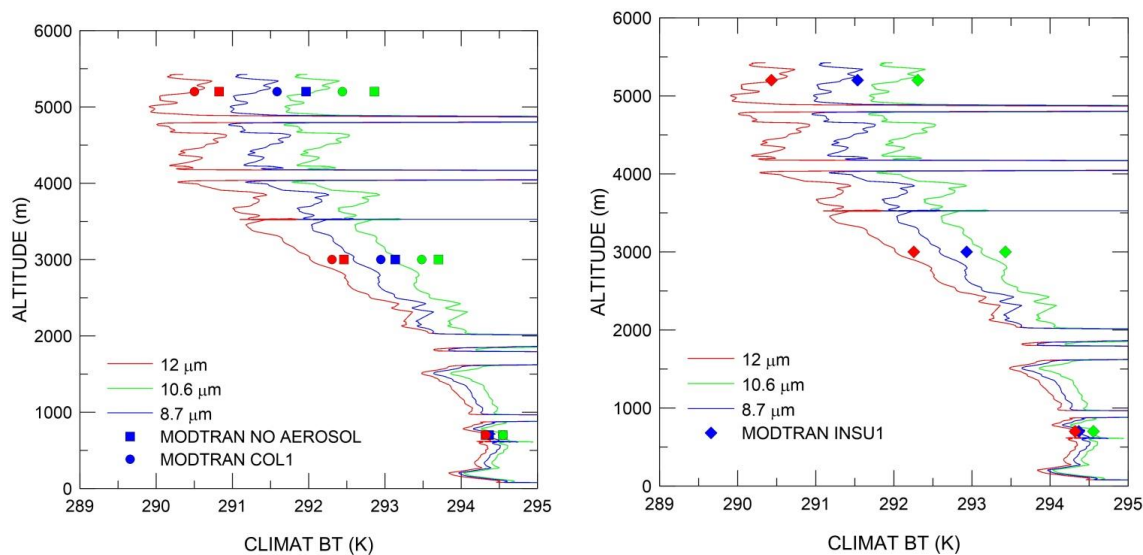
Figure 9: Same as Figure 7, but for profile F38. The simulations are made for *in situ* SD and Tunisian dust RI in the right plot.
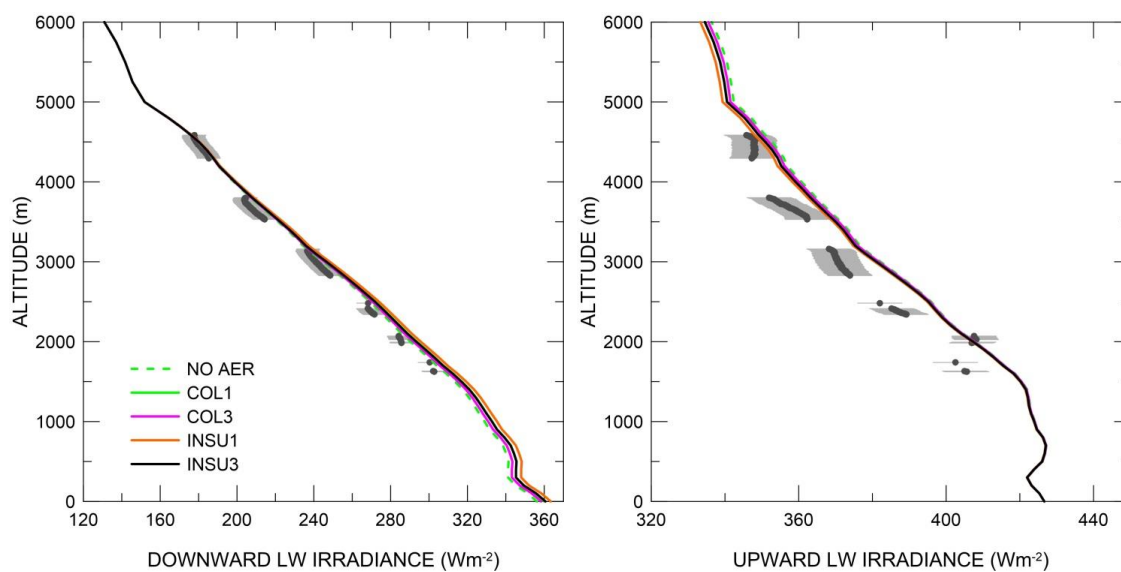
Figure 10: Same as Figure 6, but for profile F42.
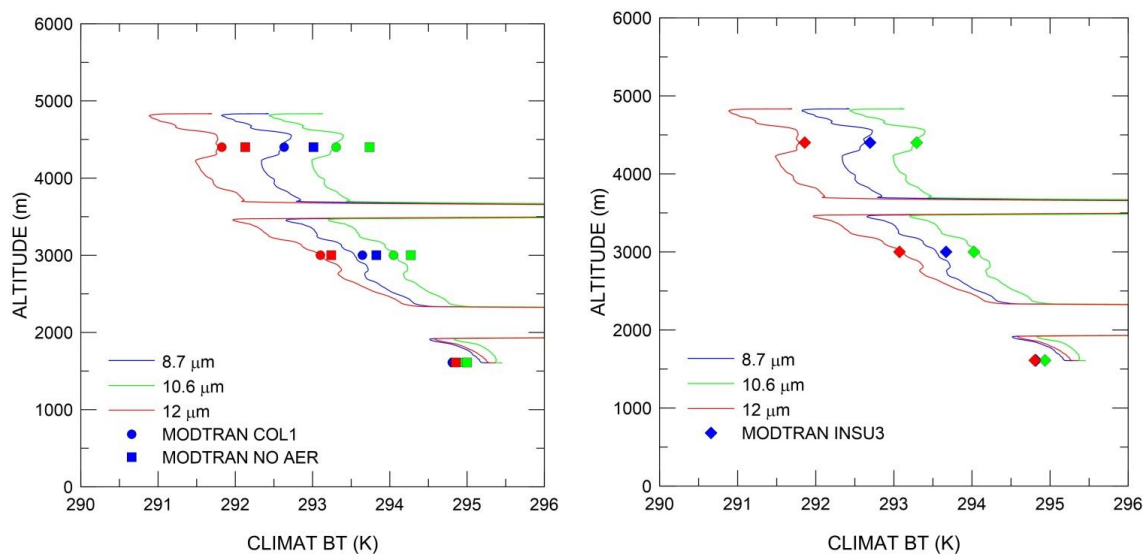
Figure 11: Same as Figure 9, but for profile F42. Simulated data are for the *in situ* SD and Tunisian and Moroccan dust RIs in the right panel.
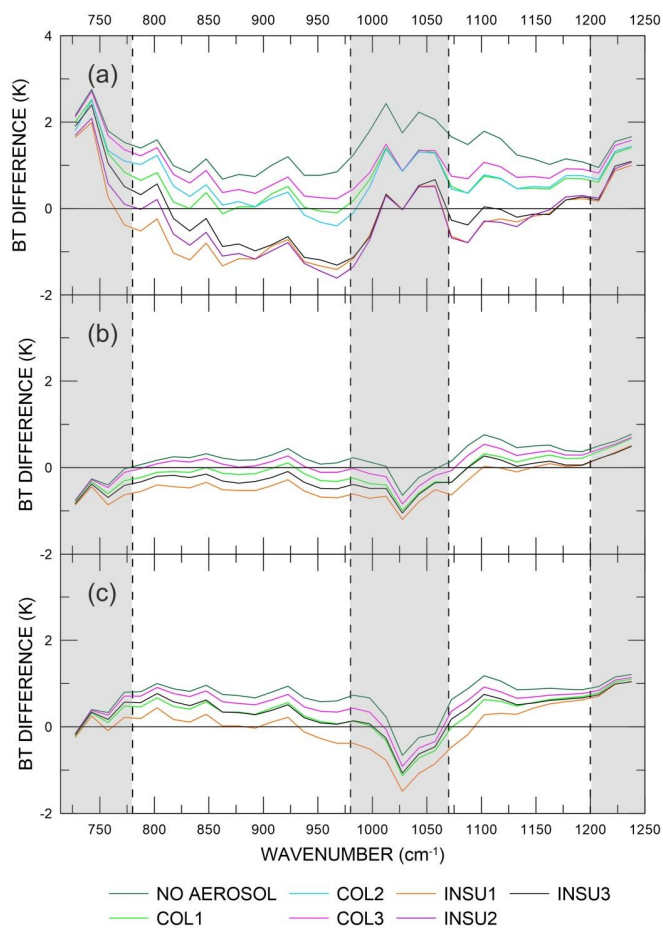
Figure 12: Differences between modelled and measured IASI BT spectra at TOA for (a) 22 June, (b) 28 June, and (c) 3 July. Simulations have been performed with different AOPs and sampled at 15 cm⁻¹ intervals. The vertical black dashed lines delimit the two spectral intervals (780-980 cm⁻¹ and 1070-1200 cm⁻¹) where the differences are discussed, while the shaded area are not considered in the analysis.
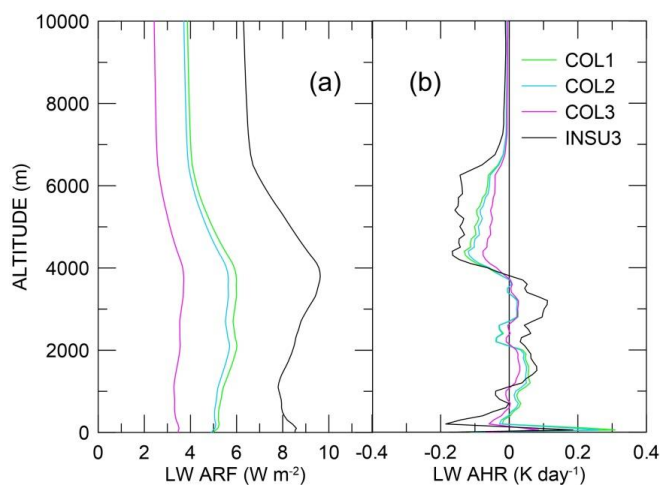
Figure 13: Dust LW radiative forcing (a) and heating rate (b) on 22 June calculated with different AOPs.